Elasto-plastic multi-fixed smeared crack model for concrete

José Sena Cruz, Joaquim Barros and Álvaro Azevedo

Report 04-DEC/E-05

Date: June of 2004

N. of pages: 70

Keywords: Concrete, numerical model, smeared crack, plasticity

Universidade do Minho

Escola de Engenharia
Departamento de Engenharia Civil

Universidade do Porto

Faculdade de Engenharia

FEUP

INDEX

NOTATION

D^{I}	Mode I stiffness modulus
D^{II}	Mode II stiffness modulus
$\underline{D}^{cr}$	Crack constitutive matrix
$\underline{D}^{e}$	Elastic constitutive matrix
$\underline{D}^{ecr}$	Elasto-cracked constitutive matrix
$\underline{D}^{ep}$	Elasto-plastic constitutive matrix
E_c	Young's modulus of concrete
G_c	Shear modulus of concrete
G_f	Mode I fracture energy of concrete
$\underline{T}^{cr}$	Transformation matrix of a crack
$f\left(\underline{\sigma},\kappa\right)=0$	Yield surface
f_c	Compressive strength of concrete
f_{ct}	Tensile strength of concrete
h	Crack band-width, Hardening modulus
h_c	Scalar parameter that amplifies the plastic strain vector
m	Number of critical crack status changes
n	Combination
n_{cr}	Number of distinct smeared crack orientations at each integration point
p	Hydrostatic pressure
q	Iteration
$\Delta\underline{\varepsilon}$	Incremental strain vector
$\Delta\underline{\varepsilon}_{\ell}^{cr}$	Incremental crack strain vector (in *CrCS*)
$\Delta\underline{\sigma}_{\ell}^{cr}$	Incremental crack stress vector (in *CrCS*)
α_{th}	Threshold angle
β	Shear retention function
γ_t^{cr}	Crack shear strain

$\underline{\varepsilon}$	Strain vector
$\underline{\varepsilon}^{cr}$	Crack strain vector
$\underline{\varepsilon}_{\ell}^{cr}$	Crack strain vector (in *CrCS*)
ε_{n}^{cr}	Crack normal strain
θ	Angle between the x_1 global axis and the crack normal axis
κ	Hardening parameter
σ_{n}^{cr}	Crack normal stress
τ_{t}^{cr}	Crack shear stress
$\underline{\sigma}$	Stress vector
$\bar{\sigma}$	Yield stress
$\underline{\sigma}_{\ell}^{cr}$	Crack stress vector (in *CrCS*)
ν_{c}	Poisson's ratio of concrete

1 INTRODUCTION

The finite element method is the basis of a powerful computational tool, which can be used to simulate the response of structures, structural components and materials, when submitted to a specified load. This tool has been extensively used to assess the behavior of concrete structures.

In order to simulate the structural response of concrete structures under the finite element framework, a mathematical idealization of the material behavior is required. This mathematical approach is commonly named constitutive or material model, and provides the relation between the stress and strain tensors in a material point of the body. In order to predict with high accuracy the behavior of concrete structures, appropriate constitutive models must be used. These constitutive models must be capable of simulating the most relevant nonlinear phenomena of the intervening materials.

The nonlinear fracture mechanics theory has been used to simulate the quasi-brittle failure of concrete (ACI 1991, ACI 1997). The discrete and the smeared crack concepts are the most used to model the concrete fracture under the framework of the finite element method. For concrete structures with a reinforcement ratio that assures crack stabilization, the smeared crack approach is more appropriate than the discrete approach, since several cracks can be formed in the structure. The discrete approach is especially suitable to simulate concrete structures where the failure is governed by the occurrence of a small number of cracks with a path that can be predicted. The discrete approach is not treated in the present work. Nevertheless, a comprehensive description of the discrete approach can be found elsewhere, e.g., Ngo and Scordelis (1967), Hillerborg et al. (1976), Rots (1988) and Bittencourt et al. (1992).

In smeared crack models, the fracture process is initiated when the maximum principal stress in a material point exceeds its tensile strength. The crack propagation is mainly controlled by the shape of the tensile-softening diagram and the material fracture energy. In order to assure mesh objectivity, the energy dissipated in the crack propagation process is associated with a characteristic length of the finite element (Bazant and Oh 1983). In the original smeared crack or single-fixed smeared crack concept, the orientation of the crack, i.e., the direction which is normal to the crack plane is coincident with the maximum principal stress orientation at crack initiation, and remains fixed

throughout the loading process. However, due to aggregate interlock and dowel action of the reinforcement (Chen 1982), the principal stresses can change their orientation and, once more, exceed the tensile strength. In this case, the single-fixed smeared crack approach predicts a numerical response that is stiffer than the experimental observations. To avoid this inconvenience, rotating single smeared crack or multi-fixed smeared crack models have been developed. In the former, the local crack coordinate system is continuously rotating with the modification of the direction of the principal axes. In the multi-fixed smeared crack models, several fixed smeared cracks are allowed to form, according to a crack initiation criterion.

Plasticity theory has been extensively used to model the concrete behavior, particularly under compressive states of stress (ASCE 1982, Chen and Han 1988). Plasticity theory is based on a micromechanical or a phenomenological approach. In the micromechanical approach, also named fundamental approach, the constitutive relations are established for the microstructural behavior. In contrast, the phenomenological approach, also known as the mathematical theory of plasticity, establishes the constitutive model directly based on observed features from experimental tests. Plasticity theory is a natural constitutive description for metals (Hill 1950), but it can also be used for cementitious materials. In the 1980s several tools were developed for mathematical plasticity, e.g., implicit Euler backward algorithms and consistent tangent operators (e.g., Ortiz and Popov 1985, Simo and Taylor 1985), which made this theory even more attractive to model the concrete behavior.

Hybrid models derived from fracture mechanics and plasticity theories have been proposed by several researchers. In these models, fracture mechanics theory is used to simulate the tensile post-cracking behavior of concrete, whereas plasticity theory is used to simulate its compressive behavior. Elasto-plastic multi-fixed smeared crack models seem to be suitable for the simulation of concrete structures, but due to their conceptual complexities and severe computational difficulties, only a few researchers were successful in the implementation of these models (de Borst and Nauta 1985, Crisfield and Wills 1989, Barros 1995).

The present report details the developed elasto-plastic multi-fixed smeared crack model. The description of the model is divided in three parts: the first part deals with the

smeared crack model; the second describes the elasto-plastic model; and, finally, the third part presents the elasto-plastic multi-fixed smeared crack model. The developed numerical model is validated with results available in the literature.

2 CRACK CONCEPTS

In this section, firstly, the single-fixed smeared crack concept is described, followed by the generalization to the multi-fixed smeared crack concept. The most relevant algorithmic aspects are detailed. Finally, the developed numerical model is validated using results available in the literature.

2.1 Smeared crack concept

After crack initiation, the basic assumption of smeared crack models, is the decomposition of the incremental strain vector, $\Delta\underline{\varepsilon}$, into an incremental crack strain vector, $\Delta\underline{\varepsilon}^{cr}$, and an incremental strain vector of the concrete between cracks, $\Delta\underline{\varepsilon}^{co}$:

$$\Delta\underline{\varepsilon} = \Delta\underline{\varepsilon}^{cr} + \Delta\underline{\varepsilon}^{co} \tag{1}$$

The decomposition expressed by (1) has been adopted by several researchers (Litton 1974, Bazant and Gambarova 1980, de Borst and Nauta 1985, Rots et al. 1985, Rots 1988).

2.1.1 Crack strains and crack stresses

Figure 1 shows the morphology of a crack for the case of plane stress. Two relative displacements define the relative movement of the crack lips: crack opening displacement, w, and crack sliding displacement, s. Axes n and t define the local coordinate system of the crack (*CrCS*), being n and t the crack normal and tangential directions, respectively.

In the smeared crack approach w is replaced with a crack normal strain defined in *CrCS*, ε_n^{cr}, and s is replaced with a crack shear strain in *CrCS*, γ_t^{cr}. The same approach can be applied to the incremental normal and shear crack strains ($\Delta\varepsilon_n^{cr}$ and $\Delta\gamma_t^{cr}$). The incremental crack strain vector in *CrCS*, $\Delta\underline{\varepsilon}_\ell^{cr}$, is defined by

$$\Delta\underline{\varepsilon}_{\ell}^{cr} = \left[\Delta\varepsilon_{n}^{cr} \quad \Delta\gamma_{t}^{cr}\right]^{T} \tag{2}$$

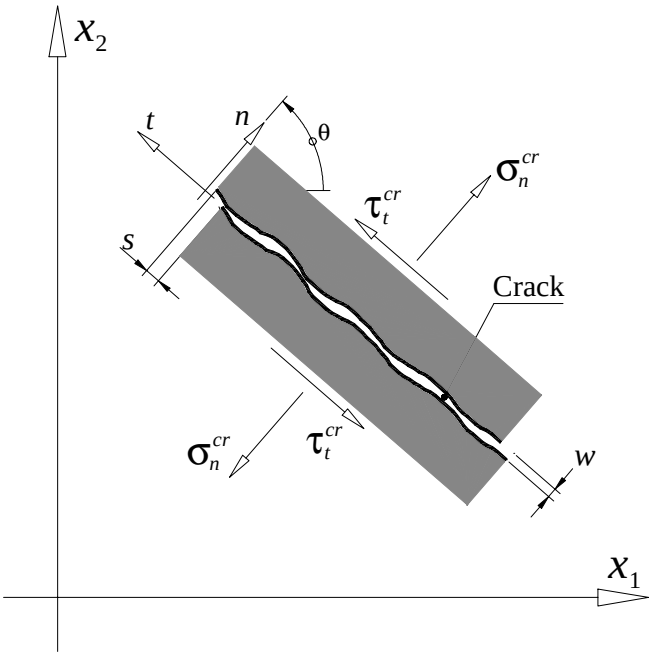

Figure 1 – Crack stresses, relative displacements and local coordinate system of the crack.

The incremental crack strain vector in the global coordinate system (*GCS*), $\Delta\underline{\varepsilon}^{cr}$, has the following three components,

$$\Delta\underline{\varepsilon}^{cr} = \left[\Delta\varepsilon_{1}^{cr} \quad \Delta\varepsilon_{2}^{cr} \quad \Delta\gamma_{12}^{cr}\right]^{T} \tag{3}$$

The transformation of the incremental crack strain vector from *CrCS* to *GCS* reads

$$\begin{bmatrix} \Delta\varepsilon_{1}^{cr} \\ \Delta\varepsilon_{2}^{cr} \\ \Delta\gamma_{12}^{cr} \end{bmatrix} = \begin{bmatrix} \cos^{2}\theta & -\sin\theta\cos\theta \\ \sin^{2}\theta & \sin\theta\cos\theta \\ 2\sin\theta\cos\theta & \cos^{2}\theta - \sin^{2}\theta \end{bmatrix} \begin{bmatrix} \Delta\varepsilon_{n}^{cr} \\ \Delta\gamma_{t}^{cr} \end{bmatrix} \tag{4}$$

or

$$\Delta\underline{\varepsilon}^{cr} = \left[\underline{T}^{cr}\right]^{T} \Delta\underline{\varepsilon}_{\ell}^{cr} \tag{5}$$

being $\left[\underline{T}^{cr}\right]^T$ the crack strain transformation matrix and θ the angle between x_1 and n (see Figure 1). The incremental local crack stress vector, $\Delta\underline{\sigma}_{\ell}^{cr}$, is defined by

$$\Delta\underline{\sigma}_{\ell}^{cr} = \left[\Delta\sigma_n^{cr} \quad \Delta\tau_t^{cr}\right]^T \tag{6}$$

where $\Delta\sigma_n^{cr}$ and $\Delta\tau_t^{cr}$ are the incremental crack normal and shear stresses, respectively. The relationship between $\Delta\underline{\sigma}_{\ell}^{cr}$ and the incremental stress vector (in *GCS*), $\Delta\underline{\sigma}$, can be defined as

$$\begin{bmatrix}\Delta\sigma_n^{cr}\\ \Delta\tau_t^{cr}\end{bmatrix} = \begin{bmatrix}\cos^2\theta & \sin^2\theta & 2\sin\theta\cos\theta\\ -\sin\theta\cos\theta & \sin\theta\cos\theta & \cos^2\theta-\sin^2\theta\end{bmatrix}\begin{bmatrix}\Delta\sigma_1\\ \Delta\sigma_2\\ \Delta\tau_{12}\end{bmatrix} \tag{7}$$

or

$$\Delta\underline{\sigma}_{\ell}^{cr} = \underline{T}^{cr}\Delta\underline{\sigma} \tag{8}$$

2.1.2 Concrete constitutive law

Assuming linear elastic behavior for the concrete between cracks (undamaged concrete), the constitutive relationship between $\Delta\underline{\varepsilon}^{co}$ and $\Delta\underline{\sigma}$ is given by,

$$\Delta\underline{\sigma} = \underline{D}^{co}\Delta\underline{\varepsilon}^{co} \tag{9}$$

where $\underline{D}^{co}$ is the constitutive matrix according to Hooke's law,

$$\underline{D}^{co} = \frac{E_c}{1-\nu^2}\begin{bmatrix}1 & \nu & 0\\ \nu & 1 & 0\\ 0 & 0 & (1-\nu)/2\end{bmatrix} \tag{10}$$

being E_c and ν the Young's modulus and Poisson's ratio of plain concrete, respectively.

2.1.3 Constitutive law of the crack

In a similar way, a relationship between $\Delta\underline{\sigma}_{\ell}^{cr}$ and $\Delta\underline{\varepsilon}_{\ell}^{cr}$ is established to simulate the crack opening and the shear sliding using a crack constitutive matrix, $\underline{D}^{cr}$,

$$\Delta\underline{\sigma}_{\ell}^{cr} = \underline{D}^{cr}\Delta\underline{\varepsilon}_{\ell}^{cr} \tag{11}$$

where $\underline{D}^{cr}$ is a 2×2 matrix including mode I and mode II crack fracture parameters.

2.1.4 Constitutive law of the cracked concrete

Combining the equations presented in the previous sections, a constitutive law of the cracked concrete is obtained. Hence, incorporating equations (1) and (5) into (9) yields,

$$\Delta\underline{\sigma} = \underline{D}^{co}\left(\Delta\underline{\varepsilon} - \left[\underline{T}^{cr}\right]^{T}\Delta\underline{\varepsilon}_{\ell}^{cr}\right) \tag{12}$$

Pre-multiplying both members of equation (12) by $\underline{T}^{cr}$ leads to

$$\underline{T}^{cr}\Delta\underline{\sigma} = \underline{T}^{cr}\underline{D}^{co}\Delta\underline{\varepsilon} - \underline{T}^{cr}\underline{D}^{co}\left[\underline{T}^{cr}\right]^{T}\Delta\underline{\varepsilon}_{\ell}^{cr} \tag{13}$$

Substituting (8) into the left side of (13) yields

$$\Delta\underline{\sigma}_{\ell}^{cr} + \underline{T}^{cr}\underline{D}^{co}\left[\underline{T}^{cr}\right]^{T}\Delta\underline{\varepsilon}_{\ell}^{cr} = \underline{T}^{cr}\underline{D}^{co}\Delta\underline{\varepsilon} \tag{14}$$

Including (11) into the left side of (14), the following equation defining the incremental crack strain vector in *CrCS* is obtained

$$\Delta\underline{\varepsilon}_{\ell}^{cr} = \left(\underline{D}^{cr} + \underline{T}^{cr}\underline{D}^{co}\left[\underline{T}^{cr}\right]^{T}\right)^{-1}\underline{T}^{cr}\underline{D}^{co}\Delta\underline{\varepsilon} \tag{15}$$

The inclusion of (15) in (12) leads to the constitutive law of the cracked concrete, which reads

$$\Delta\underline{\sigma} = \left(\underline{D}^{co} - \underline{D}^{co}\left[\underline{T}^{cr}\right]^{T}\left(\underline{D}^{cr} + \underline{T}^{cr}\underline{D}^{co}\left[\underline{T}^{cr}\right]^{T}\right)^{-1}\underline{T}^{cr}\underline{D}^{co}\right)\Delta\underline{\varepsilon} \tag{16}$$

or

$$\Delta\underline{\sigma} = \underline{D}^{crco}\Delta\underline{\varepsilon} \tag{17}$$

where $\underline{D}^{crco}$ is the following constitutive matrix for the cracked concrete

$$\underline{D}^{crco} = \underline{D}^{co} - \underline{D}^{co}\left[\underline{T}^{cr}\right]^{T}\left(\underline{D}^{cr} + \underline{T}^{cr}\underline{D}^{co}\left[\underline{T}^{cr}\right]^{T}\right)^{-1}\underline{T}^{cr}\underline{D}^{co} \tag{18}$$

2.1.5 Crack fracture parameters

In the present model, the crack constitutive matrix, $\underline{D}^{cr}$, is assumed to be diagonal

$$\underline{D}^{cr} = \begin{bmatrix} D_{I}^{cr} & 0 \\ 0 & D_{II}^{cr} \end{bmatrix} \tag{19}$$

In this matrix D_{I}^{cr} and D_{II}^{cr} are the mode I and mode II stiffness modulus associated with the crack behavior.

The crack-dilatancy effect and the shear-normal stress coupling is not considered in the present approach. The shear-normal stress coupling, however, may be simulated indirectly, allowing non-orthogonal cracks to form and relating D_{II}^{cr} with the crack normal strain (Rots 1988). This strategy is adopted in the present model.

The crack initiation in the present model is governed by the Rankine yield surface (see Figure 2), i.e., when the maximum principal stress, σ_{I}, exceeds the uniaxial tensile strength, f_{ct}, a crack is formed. This assumption is justified by the experimental results obtained by Kupfer et al. (1969) when the tensile cracking is not accompanied by significant lateral compression.

According to Rots (1988), the most suitable approach to simulate the crack propagation under the finite element framework is by taking into account the concrete fracture parameters, namely, the shape of the tensile-softening diagram and the fracture energy.

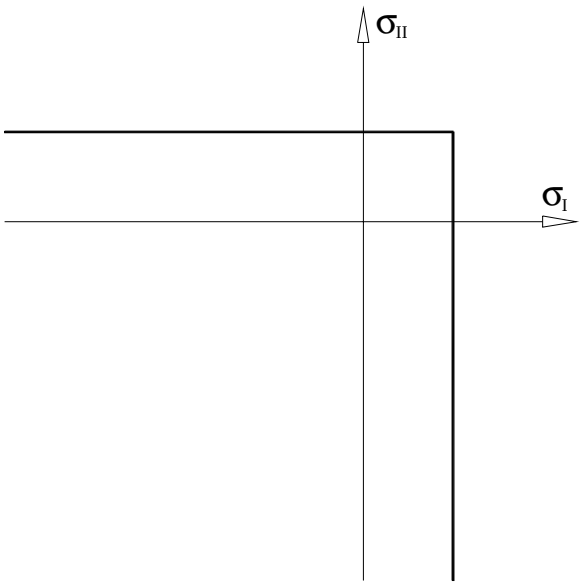

Figure 2 – Rankine yield surface in the 2D principal stress space.

Two distinct tensile-softening diagrams are available in the developed computational code: tri-linear and exponential diagrams (see Figure 3). The tri-linear diagram shown in Figure 3(a) is defined by the following expressions

$$\sigma_n^{cr}\left(\varepsilon_n^{cr}\right)=\begin{cases} f_{ct}+D_{I,1}^{cr}\varepsilon_n^{cr} & if\ \ 0<\varepsilon_n^{cr}\le\xi_1\varepsilon_{n,ult}^{cr} \\ \alpha_1 f_{ct}+D_{I,2}^{cr}\left(\varepsilon_n^{cr}-\xi_1\varepsilon_{n,ult}^{cr}\right) & if\ \ \xi_1\varepsilon_{n,ult}^{cr}<\varepsilon_n^{cr}\le\xi_2\varepsilon_{n,ult}^{cr} \\ \alpha_2 f_{ct}+D_{I,3}^{cr}\left(\varepsilon_n^{cr}-\xi_2\varepsilon_{n,ult}^{cr}\right) & if\ \ \xi_2\varepsilon_{n,ult}^{cr}<\varepsilon_n^{cr}\le\varepsilon_{n,ult}^{cr} \\ 0 & if\ \ \varepsilon_n^{cr}>\varepsilon_{n,ult}^{cr} \end{cases} \tag{20}$$

with,

$$D_{I,i}^{cr}=-k_i\frac{hf_{ct}^2}{G_f} \tag{21}$$

where

$$k_1 = \frac{(1-\alpha_1)(\xi_1 + \alpha_1\xi_2 - \alpha_2\xi_1 + \alpha_2)}{2\xi_1}$$
$$k_2 = \frac{(\alpha_1 - \alpha_2)(\xi_1 + \alpha_1\xi_2 - \alpha_2\xi_1 + \alpha_2)}{2(\xi_2 - \xi_1)} \quad (22)$$
$$k_3 = \frac{\alpha_2(\xi_1 + \alpha_1\xi_2 - \alpha_2\xi_1 + \alpha_2)}{2(1-\xi_2)}$$

The ultimate crack normal strain, $\varepsilon_{n,ult}^{cr}$, is given by,

$$\varepsilon_{n,ult}^{cr} = k_4 \frac{G_f}{f_{ct} h} \quad (23)$$

where

$$k_4 = \frac{2}{\xi_1 + \alpha_1\xi_2 - \alpha_2\xi_1 + \alpha_2} \quad (24)$$

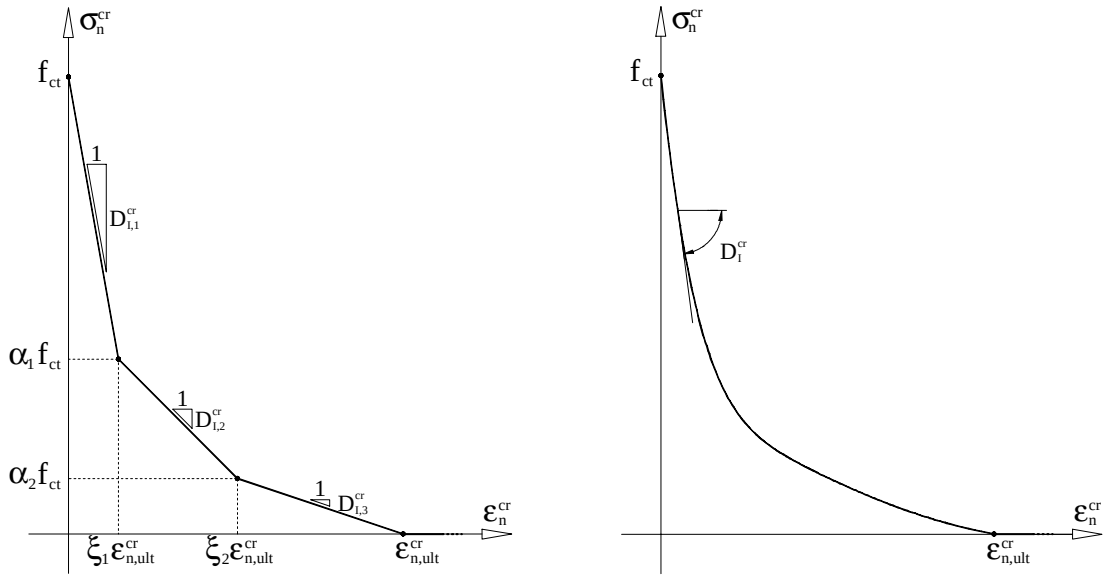

(a) (b)

Figure 3 – Tensile-softening diagrams: tri-linear (a) and exponential (b).

The exponential softening diagram proposed by Cornelissen et al. (1986) (see Figure 3(b)) is defined by

$$\frac{\sigma_n^{cr}\left(\varepsilon_n^{cr}\right)}{f_{ct}} = \\ = \begin{cases} \left(1+\left(C_1\dfrac{\varepsilon_n^{cr}}{\varepsilon_{n,ult}^{cr}}\right)^3\right)\exp\left(-C_2\dfrac{\varepsilon_n^{cr}}{\varepsilon_{n,ult}^{cr}}\right)-\dfrac{\varepsilon_n^{cr}}{\varepsilon_{n,ult}^{cr}}\left(1+C_1^3\right)\exp(-C_2) & if\ \ 0<\varepsilon_n^{cr}<\varepsilon_{n,ult}^{cr} \\ 0 & if\ \ \varepsilon_n^{cr}\geq\varepsilon_{n,ult}^{cr} \end{cases} \tag{25}$$

where $C_1 = 3.0$ and $C_2 = 6.93$. The ultimate crack normal strain, $\varepsilon_{n,ult}^{cr}$, is obtained from,

$$\varepsilon_{n,ult}^{cr} = \frac{1}{k}\frac{G_f}{f_{ct}h} \tag{26}$$

where

$$k = \left[\frac{1}{C_2}\left[1+6\left(\frac{C_1}{C_2}\right)^3\right]-\left[\frac{1}{C_2}+C_1^3\left(\frac{1}{C_2}+\frac{3}{C_2^2}+\frac{6}{C_2^3}+\frac{6}{C_2^4}\right)+\frac{1}{2}\left(1+C_1^3\right)\right]\right]\exp\left(-C_2\right) \tag{27}$$

The mode I crack stiffness modulus is calculated with the following expression

$$D_I^{cr} = f_{ct}\left[3\left(C_1\frac{\varepsilon_n^{cr}}{\varepsilon_{n,ult}^{cr}}\right)^2\frac{C_1}{\varepsilon_{n,ult}^{cr}}\exp\left(-C_2\frac{\varepsilon_n^{cr}}{\varepsilon_{n,ult}^{cr}}\right)+ \right. \\ \left. \exp\left(-C_2\frac{\varepsilon_n^{cr}}{\varepsilon_{n,ult}^{cr}}\right)\left(-C_2\frac{\varepsilon_n^{cr}}{\varepsilon_{n,ult}^{cr}}\right)\left[1+\left(C_1\frac{\varepsilon_n^{cr}}{\varepsilon_{n,ult}^{cr}}\right)^3\right]-\frac{1+C_1^3}{\varepsilon_{n,ult}^{cr}}\exp\left(-C_2\right)\right] \tag{28}$$

The concrete fracture energy, G_f, is the energy required to propagate a tensile crack of unit area. Generally, G_f is assumed to be a material parameter and according to the CEB-FIB model code (1993) it can be estimated from the concrete compressive strength, f_c, and maximum aggregate size.

In the smeared crack approach, the fracture zone is distributed in a certain width of the finite element, which is designated crack band-width, h, as indicated in Figure 4. In this model a constant strain distribution in the width h is assumed. To assure mesh

objectivity, the concrete fracture energy and the crack band-width must be mesh dependent. Several researchers have proposed different ways to estimate h (Bazant and Oh 1983, Rots 1985, Leibengood et al. 1986, Oñate et al. 1987, Dahlblom and Ottosen 1990, Oliver et al. 1990, Cervenka et al. 1990, Rots 1992, Feenstra 1993). In the present numerical model, the crack band-width can be estimated in three different ways: equal to the square root of the area of the finite element, equal to the square root of the area of the integration point or equal to a constant value. To avoid *snap-back instability*, the crack band-width is subjected to the following constraint (de Borst 1991),

$$h \leq \frac{G_f E_c}{b\, f_{ct}^2} \tag{29}$$

where $b = \max\{k_i\}$ for tri-linear softening and $b = k\left(C_2 + \left(1 + C_1^3\right)\exp\left(-C_2\right)\right)$ for exponential softening.

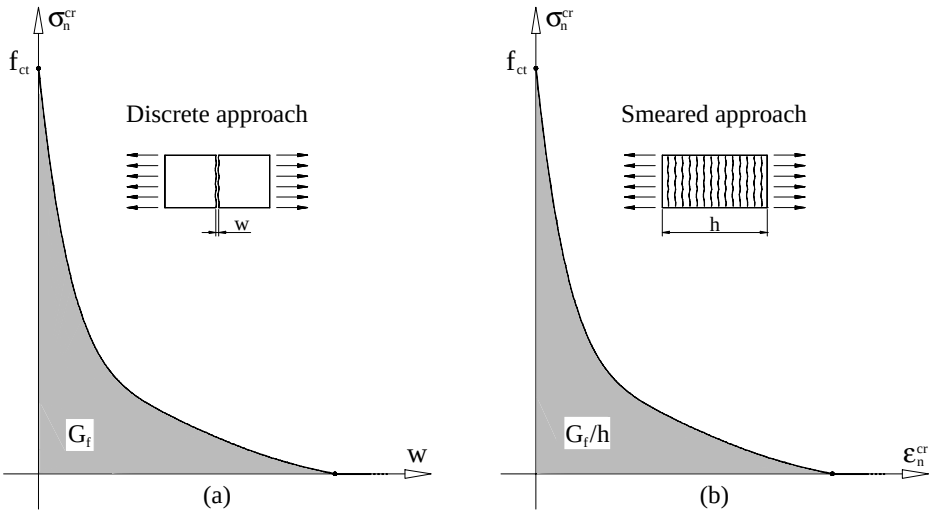

Figure 4 – Two distinct approaches to model the tensile-softening diagram: discrete (a) and smeared (b) crack models.

Applying the strain decomposition concept to the crack fracture mode II, yields

$$\Delta\gamma = \Delta\gamma^{cr} + \Delta\gamma^{co} \tag{30}$$

or,

$$\frac{1}{\beta G_c} = \frac{1}{D_{II}^{cr}} + \frac{1}{G_c} \tag{31}$$

resulting

$$D_{II}^{cr} = \frac{\beta}{1-\beta} G_c \tag{32}$$

D_{II}^{cr} is the mode II crack fracture stiffness modulus. The parameter β is called the shear retention factor and its value depends on the crack normal strain and on the ultimate crack normal strain (Rots 1988, Póvoas 1991, Barros 1995),

$$\beta = \left(1 - \frac{\varepsilon_n^{cr}}{\varepsilon_{n,ult}^{cr}}\right)^{p_1} \tag{33}$$

In this equation p_1 is an integer parameter that, currently, can assume the values of 1, 2 or 3 (Barros 1995). When $\varepsilon_n^{cr} = 0$ (closed crack) a full interlock is assumed. For a fully open crack ($\varepsilon_n^{cr} \geq \varepsilon_{n,ult}^{cr}$) the shear retention factor is equal to zero, resulting in a null crack shear stiffness that corresponds to a negligible aggregate interlock.

2.2 Multi-fixed smeared crack concept

In the previous sections the concept of the fixed smeared crack model was described. In this model only one fixed smeared crack was allowed to form at each integration point. To be capable of simulating the formation of more than one fixed smeared crack, as well as, to be not restricted to the particular case of two orthogonal cracks (Azevedo 1985, Póvoas 1991), the formulation was extended, resulting in the multi-fixed smeared crack model.

To deal with the eventual formation of n_{cr} smeared cracks at each integration point, the generalized crack transformation matrix, $\underline{T}^{cr}$, and the crack constitutive matrix, $\underline{D}^{cr}$, adopt the following format

$$\underline{T}^{cr} = \left[\underline{T}_1^{cr}(\theta_1) \quad \underline{T}_2^{cr}(\theta_2) \quad \ldots \quad \underline{T}_{n_{cr}}^{cr}(\theta_{n_{cr}}) \right]^T \tag{34}$$

$$\underline{D}^{cr} = \begin{bmatrix} \underline{D}_1^{cr} & \underline{0} & \ldots & \underline{0} \\ \underline{0} & \underline{D}_2^{cr} & \ldots & \underline{0} \\ \ldots & \ldots & \ldots & \ldots \\ \underline{0} & \underline{0} & \ldots & \underline{D}_{n_{cr}}^{cr} \end{bmatrix} \tag{35}$$

In these matrices, $\underline{T}_i^{cr}(\theta_i)$ and $\underline{D}_i^{cr}$ correspond to the crack transformation matrix and to the crack constitutive matrix of the *i-th* crack, respectively. Matrix $\underline{D}^{cr}$ is diagonal since the sub-matrices $\underline{D}_i^{cr}$ have null off-diagonal terms (see Section 2.1.5).

2.2.1 Crack initiation

Cracking occurs when the maximum principal stress exceeds the concrete uniaxial tensile strength, f_{ct}. After crack initiation, and assuming that the shear retention factor is non-null, i.e., the crack shear stresses can be transferred between the crack lips, the values and the orientation of the principal stresses can change during the loading process. For this reason the maximum principal stress in the concrete between cracks can also exceed f_{ct}. In the present work a new crack is initiated when the following two conditions are satisfied simultaneously:

- the maximum principal stress, σ_I, exceeds the uniaxial tensile strength, f_{ct};
- the angle between the direction of the existing cracks and the direction of σ_I, $\overline{\theta}_I$, exceeds the value of a predefined threshold angle, α_{th}.

Typically, the threshold angle varies between 30 and 60 degrees (de Borst and Nauta 1985). When the second condition is not verified (which means that the new crack is not initiated) the tensile strength is updated in order to avoid inconsistencies in the crack

initiation process. With this strategy the updated tensile strength can significantly exceed the original concrete tensile strength (Rots 1988).

2.2.2 Crack evolution history

In a previously cracked integration point, the coupling between non-orthogonal cracks is simulated with fracture parameters associated to the new cracks. The fracture energy available for the next crack, G_f^{next}, is calculated with (Barros 1995)

$$G_f^{next} = \left(G_f - G_{f,a}\right)\left(\frac{\alpha}{\pi/2}\right)^{p_2} + G_{f,a} \tag{36}$$

where p_2 is an integer parameter and can assume the values of 1, 2 or 3, α is the angle (in radians) between the next and the previous crack and $G_{f,a}$ is the available fracture energy in the previous crack. Its value is calculated subtracting the fracture energy consumed by the previous crack, $G_{f,c}^{prev}$, from the concrete fracture energy (see Figure 5),

$$G_{f,a} = G_f - G_{f,c}^{prev} \tag{37}$$

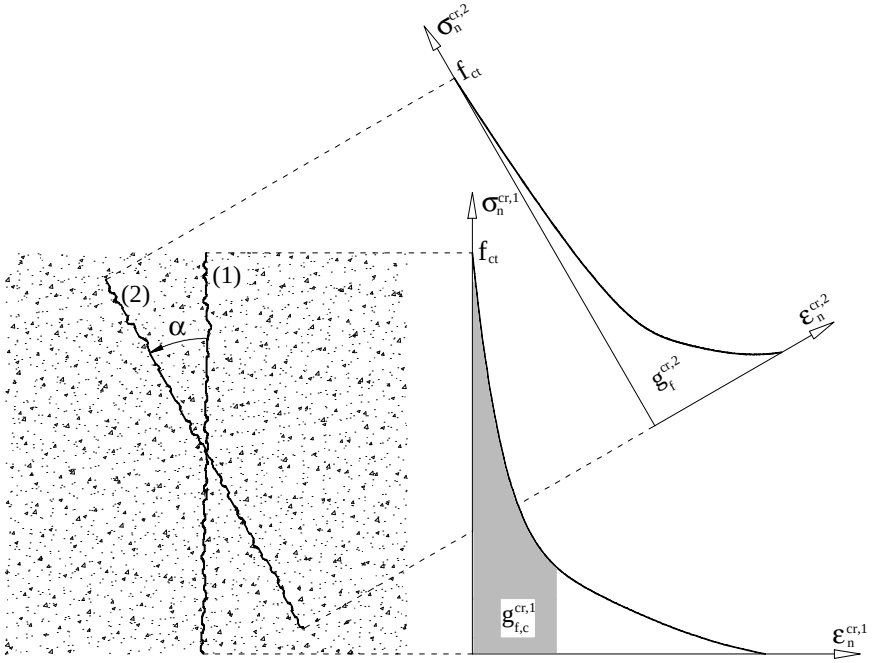

Figure 5 – Fracture energy available for the next crack.

2.3 Algorithmic aspects

In a multi-fixed smeared crack model the consideration of all the crack status changes that can occur during the loading process of a concrete element, requires the implementation of several computational procedures. Otherwise the model becomes unreliable and inefficient for practical use (de Borst and Nauta 1985, Rots 1988, Crisfield and Wills 1989, Barros 1995, Hofstetter and Mang 1995). The implementation of these algorithms in the FEMIX computer code (Azevedo et al. 2003) is described below.

2.3.1 Stress update

When the strain field in a cracked integration point is submitted to an incremental strain, $\Delta\underline{\varepsilon}_m$, the stress state of the integration point is also modified and must be updated ($\underline{\sigma}_m$). The incremental relationship (8) can be written in terms of total stresses,

$$\underline{\sigma}_{\ell,m}^{cr} = \underline{T}_m^{cr}\underline{\sigma}_m \tag{38}$$

This equation is equivalent to

$$\underline{\sigma}_{\ell,m-1}^{cr} + \Delta\underline{\sigma}_{\ell,m}^{cr} = \underline{T}_m^{cr}\left(\underline{\sigma}_{m-1} + \Delta\underline{\sigma}_m\right) \tag{39}$$

Including (12) in (39) yields

$$\underline{\sigma}_{\ell,m-1}^{cr} + \Delta\underline{\sigma}_{\ell,m}^{cr} = \underline{T}_m^{cr}\left(\underline{\sigma}_{m-1} + \underline{D}^{co}\left(\Delta\underline{\varepsilon}_m - \left[\underline{T}_m^{cr}\right]^T \Delta\underline{\varepsilon}_{\ell,m}^{cr}\right)\right) \tag{40}$$

Equation (40) can be written as

$$\underline{\sigma}_{\ell,m-1}^{cr} + \Delta\underline{\sigma}_{\ell,m}^{cr}\left(\Delta\underline{\varepsilon}_{\ell,m}^{cr}\right) + \underline{T}_m^{cr}\underline{D}^{co}\left[\underline{T}_m^{cr}\right]^T \Delta\underline{\varepsilon}_{\ell,m}^{cr} - \underline{T}_m^{cr}\underline{\sigma}_{m-1} - \underline{T}_m^{cr}\underline{D}^{co}\Delta\underline{\varepsilon}_m = \underline{0} \tag{41}$$

where $\Delta\underline{\sigma}_{\ell,m}^{cr}$ depends on $\Delta\underline{\varepsilon}_{\ell,m}^{cr}$. The components of the incremental strain crack vector, $\Delta\underline{\varepsilon}_{\ell,m}^{cr}$, are the unknown variables of the nonlinear equations (41). This vector contains the two local strain components of the active cracks (non-closed cracks). To solve this

equation two different methods were implemented: the Newton-Raphson and the fixed-point iteration methods (Chapra and Canale 1998). The methods exhibiting quadratic convergence, such as the Newton-Raphson method, are usually very efficient, but in some cases the solution cannot be obtained. In theses cases the Newton-Raphson method is replaced with the fixed-point iteration method which exhibits linear convergence. In the following algorithms the first member of equation (41) is referred as a function f of $\Delta\underline{\varepsilon}_{\ell}^{cr}$, i.e.,

$$\underline{f}\left(\Delta\underline{\varepsilon}_{\ell,m}^{cr}\right)=\underline{\sigma}_{\ell,m-1}^{cr}+\Delta\underline{\sigma}_{\ell,m}^{cr}\left(\Delta\underline{\varepsilon}_{\ell,m}^{cr}\right)+\underline{T}_{m}^{cr}\underline{D}^{co}\left[\underline{T}_{m}^{cr}\right]^{T}\Delta\underline{\varepsilon}_{\ell,m}^{cr}-\underline{T}_{m}^{cr}\underline{\sigma}_{m-1}-\underline{T}_{m}^{cr}\underline{D}^{co}\Delta\underline{\varepsilon}_{m} \tag{42}$$

with this assumption, equation (41) becomes $\underline{f}\left(\Delta\underline{\varepsilon}_{\ell,m}^{cr}\right)=\underline{0}$.

Figure 6 shows the flowchart of the Newton-Raphson method adapted to the solution of (42). The calculation of the initial solution (step (2) in Figure 6) is performed with equation (41), considering $\Delta\underline{\sigma}_{\ell,m}^{cr}\left(\Delta\underline{\varepsilon}_{\ell,m}^{cr}\right)$ equal to $\underline{D}_{m-1}^{cr}\Delta\underline{\varepsilon}_{\ell,m}^{cr}$, where $\underline{D}_{m-1}^{cr}$ is the tangential crack constitutive matrix of the previous converged stress state.

In step 3 $Toler=10^{-6}f_c$, where f_c is the concrete compressive strength. The symbol $\|\ \|_{\infty}$ means the infinite norm of the vector, i.e., the maximum absolute value found in vector $\underline{f}$. The first derivatives of $\underline{f}$ in order to the incremental crack strain vector can be defined as

$$\frac{\partial\underline{f}\left(\Delta\underline{\varepsilon}_{\ell}^{cr}\right)}{\partial\Delta\underline{\varepsilon}_{\ell}^{cr}}=\underline{D}^{cr}+\hat{\underline{D}}^{cr}\Delta\underline{\varepsilon}_{\ell}^{cr}+\underline{T}^{cr}\underline{D}^{co}\left[\underline{T}^{cr}\right]^{T} \tag{43}$$

where

$$\hat{\underline{D}}^{cr}=\begin{bmatrix}\hat{\underline{D}}_{1}^{cr} & \underline{0} & \cdots & \underline{0}\\ \underline{0} & \hat{\underline{D}}_{2}^{cr} & \cdots & \underline{0}\\ \cdots & \cdots & \cdots & \cdots\\ \underline{0} & \underline{0} & \cdots & \hat{\underline{D}}_{n_{cr}}^{cr}\end{bmatrix} \tag{44}$$

and

$$\underline{\hat{D}}_i^{cr} = \begin{bmatrix} 0 & 0 \\ \left.\dfrac{\partial D_{II}^{cr}}{\partial \Delta \varepsilon_n^{cr}}\right|_i & 0 \end{bmatrix} \tag{45}$$

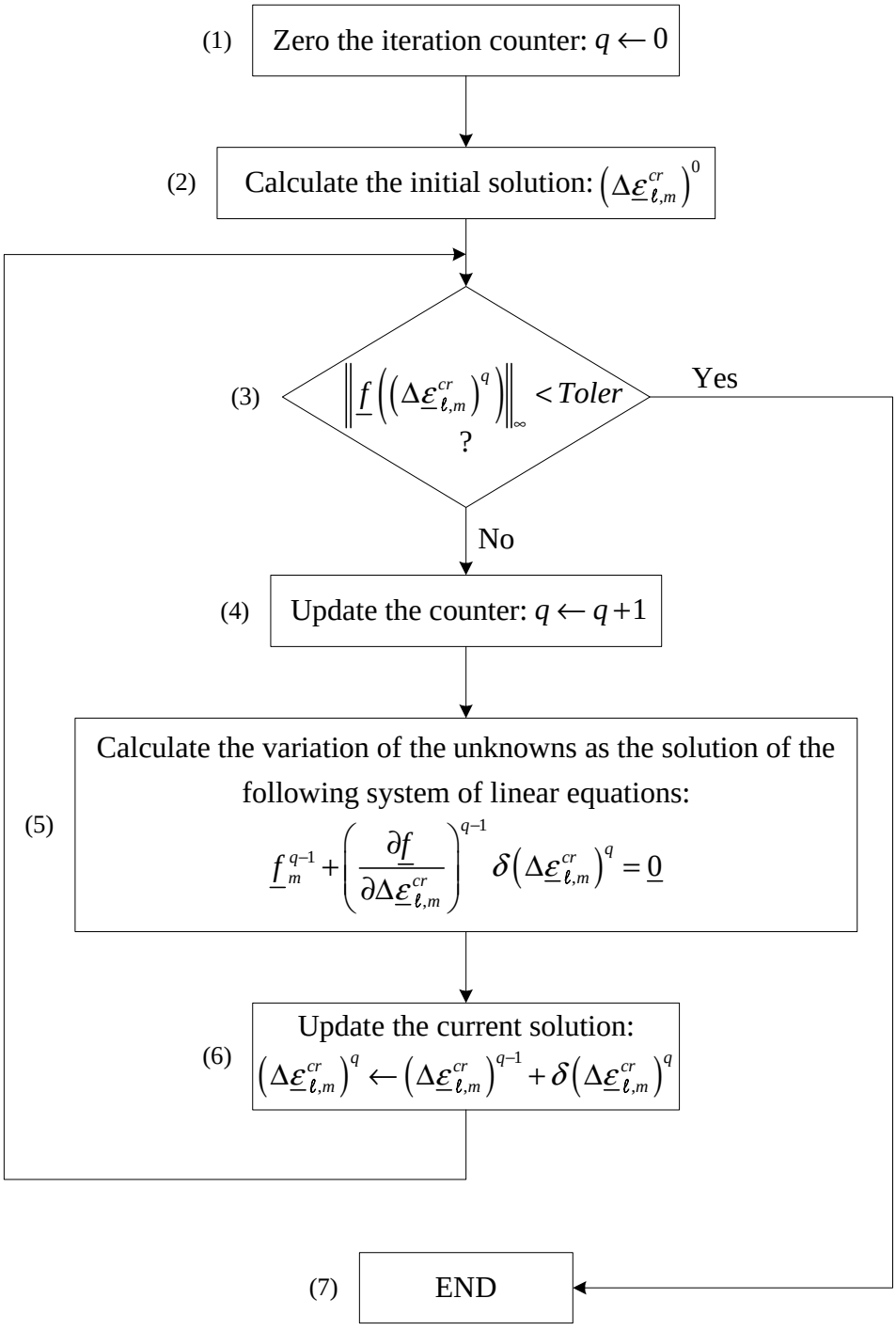

Figure 6 – Flowchart of the Newton-Raphson method.

When equation (33) is adopted to define (32) the non-null term of (45) is

$$\frac{\partial D_{II}^{cr}}{\partial \Delta \varepsilon_n^{cr}} = -\frac{\left(1-\frac{\varepsilon_n^{cr}+\Delta\varepsilon_n^{cr}}{\varepsilon_{n,ult}^{cr}}\right)^{p_1} G_c p_1}{\varepsilon_{n,ult}^{cr}\left(1-\frac{\varepsilon_n^{cr}+\Delta\varepsilon_n^{cr}}{\varepsilon_{n,ult}^{cr}}\right)\left(1-\left(1-\frac{\varepsilon_n^{cr}+\Delta\varepsilon_n^{cr}}{\varepsilon_{n,ult}^{cr}}\right)^{p_1}\right)} - \frac{\left(\left(1-\frac{\varepsilon_n^{cr}+\Delta\varepsilon_n^{cr}}{\varepsilon_{n,ult}^{cr}}\right)^{p_1}\right)^2 G_c p_1}{\left(1-\left(1-\frac{\varepsilon_n^{cr}+\Delta\varepsilon_n^{cr}}{\varepsilon_{n,ult}^{cr}}\right)^{p_1}\right)^2 \varepsilon_{n,ult}^{cr}\left(1-\frac{\varepsilon_n^{cr}+\Delta\varepsilon_n^{cr}}{\varepsilon_{n,ult}^{cr}}\right)} \quad (46)$$

When the convergence is not obtained using the Newton-Raphson method, the fixed-point iteration method, shown in Figure 7 is tried.

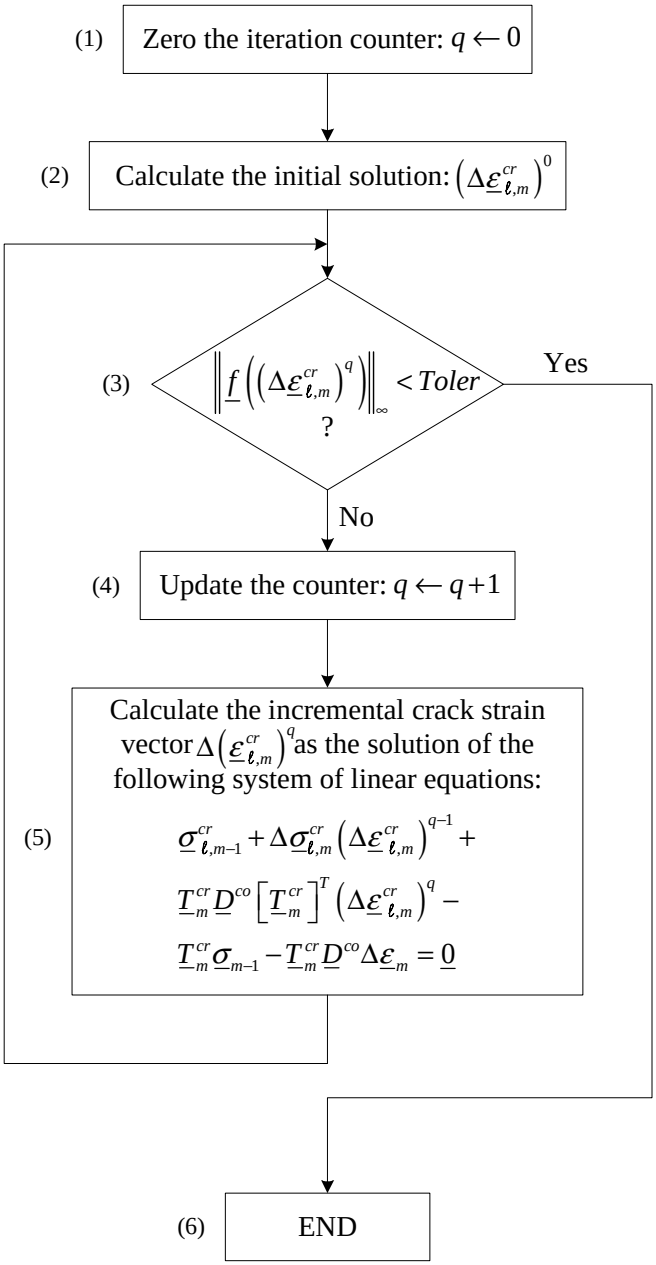

Figure 7 – Fixed-point iteration method.

2.3.2 Crack status

Depending on the followed $\sigma^{cr}_n - \varepsilon^{cr}_n$ path, a crack can assume one of six crack statuses as shown Figure 8. The first (1) was named *initiation* and corresponds to the crack initiation. The *opening* status occurs when the crack is in the softening branch (2). In the present model a secant branch is assumed to simulate the unloading (3) and the reloading (5) phases. The *closing* status designates the unloading phase while the *reopening* crack status is attributed to the crack in the reloading phase. This assumption does not correspond to the most realistic approach, since cyclic tests reveal the occurrence of an hysteretic behavior

(Hordijk 1991). Since the present model was developed to simulate the behavior of concrete structures under monotonic loading, this simple approach is sufficiently accurate. If a crack closes, i.e., $\varepsilon_n^{cr} = 0$, the crack status receives the designation of *closed* (4). The *fully open* (6) crack status occurs when in the crack the mode I fracture energy is fully exhausted.

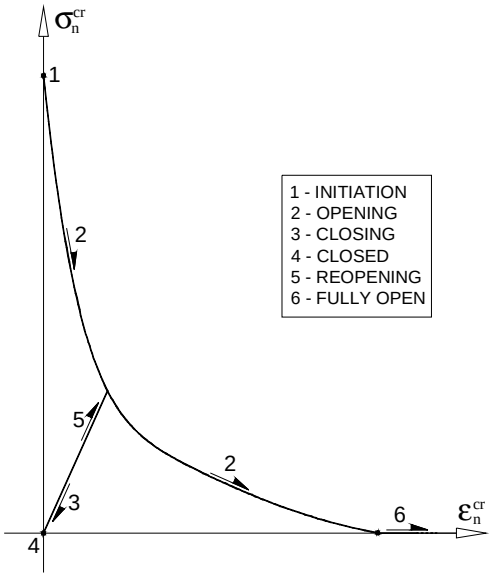

Figure 8 – Crack status.

The stress update procedure described in the previous section is only applied to the active cracks, i.e., when $\varepsilon_n^{cr} > 0$. When a crack initiates ($\sigma_I > f_{ct}$ and $\bar{\theta}_I \geq \alpha$), when a crack closes ($\varepsilon_n^{cr} < 0$) or when a closed crack reopens ($\sigma_n^{cr} > 0$), the incremental strain vector $\Delta\underline{\varepsilon}$ must be successively decomposed in order to accurately simulate the crack status evolution (see Figure 9). These three crack status changes were named critical crack status changes. This decomposition is necessary since the content of $\underline{D}^{cr}$ and $\underline{T}^{cr}$ matrices depends on the number of active cracks. For instance, when a new crack is formed the size of these matrices must be extended in order to accommodate new terms (see equations (34) and (35)).

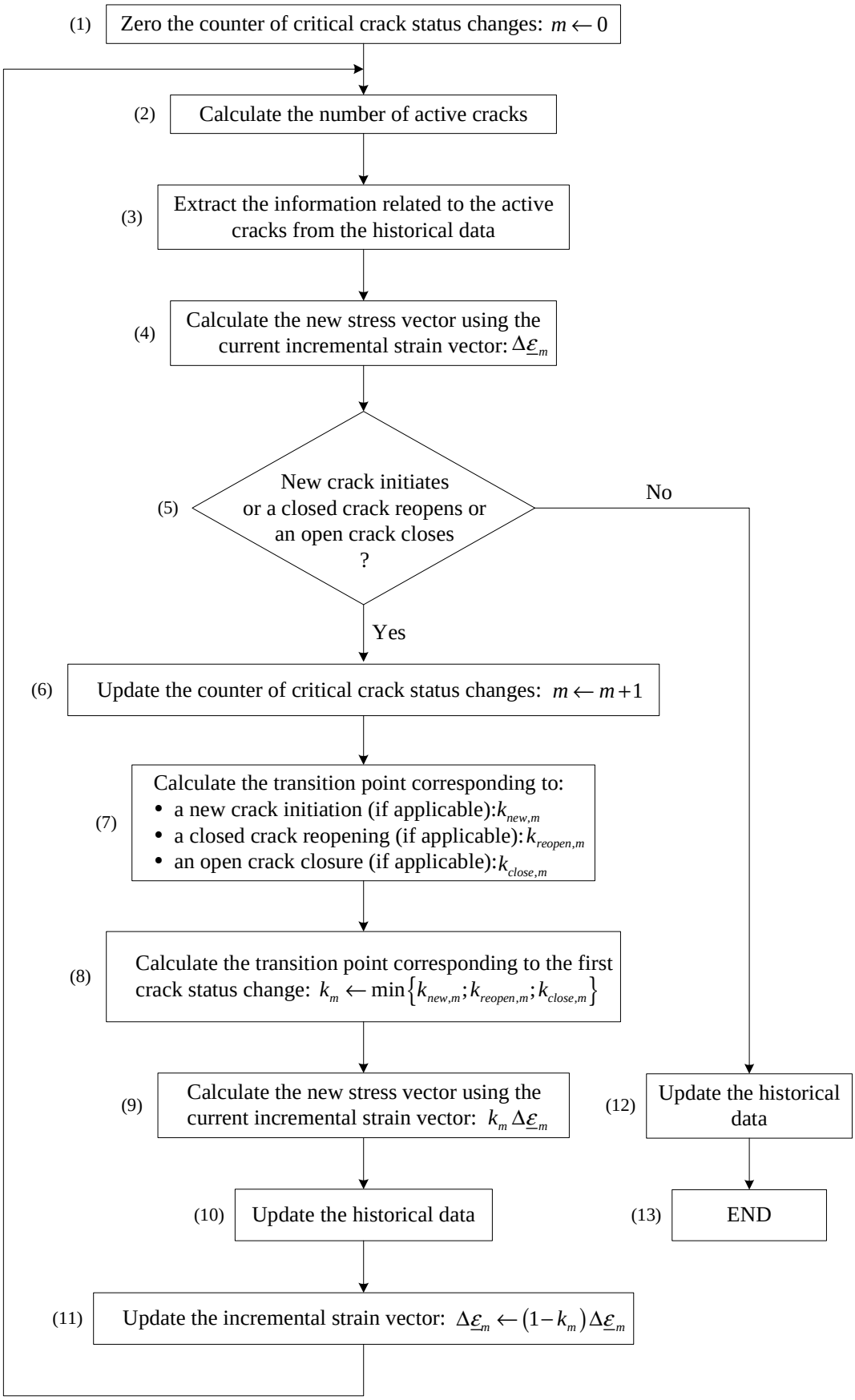

Figure 9 – Algorithm used for the decomposition of the incremental strain vector.

The calculation of the number of active cracks (step (2) in Figure 9) is based on the content of the database containing the historical data. This database stores, for each integration point and for each iteration of the incremental-iterative procedure, all the critical parameters such as the stress and strain vectors, the number of cracks, the crack stress and strain vectors, the crack statuses, the crack orientation and data associated with the crack evolution history.

The stress update procedure, described in the Section 2.3.1, is performed in step (4) of Figure 9. When one critical crack status change occurs, the current incremental strain vector, $\Delta\underline{\varepsilon}$, must be decomposed.

To calculate the transition point corresponding to crack initiation, $k_{new,m}$, to a closed crack reopening, $k_{reopen,m}$, or to an open crack closure, $k_{close,m}$, two algorithms were implemented: the Newton-Raphson method (Figure 10) and the bisection method (Figure 11). The last one is used when the first fails. Table 1 contains the definition of the function $f(k)$, the initial solution and the parameter *Toler* for some crack status changes. These functions and parameters are used in the algorithms shown in Figure 10 and Figure 11.

Table 1 – Definition of the function f used in the algorithms shown in Figure 10 and Figure 11, the initial solution and the respective convergence criterion parameter.

	Critical crack status changes		
	New crack initiation	**Closed crack reopening**	**Open crack closure**
$f(k)$	$f_{ct} - \sigma_I(k)$	$\sigma_n^{cr}(k)$	$\varepsilon_n^{cr}(k)$
k^0	$\dfrac{f_{ct} - \sigma_I^{p-1}}{\sigma_I\left(\Delta\underline{\varepsilon}^p\right) - \sigma_I^{p-1}}$	$\dfrac{\varepsilon_{n,m}^{cr}}{\varepsilon_{n,m}^{cr} - \varepsilon_{n,m-1}^{cr}}$	0.5
Toler	$10^{-6} f_c$	$10^{-6} f_c$	10^{-6}

Besides the crack initiation conditions described in Section 2.2.1 (tensile strength and threshold angle), an additional check is required. When a new crack is initiating, $k_{new,m}$ is calculated (see Figure 9). At this phase, the new crack is only considered as potential

crack. At the end of the first part of the incremental strain vector, $k_{new,m}\Delta\underline{\varepsilon}_m$, the crack normal stress, σ_n^{cr}, is equal to the current tensile strength, f_{ct}, and its normal crack strain, ε_n^{cr}, has a null value (point 1 in Figure 8). For the remaining part of the incremental strain vector, $\left(1-k_{new,m}\right)\Delta\underline{\varepsilon}_{m-1}$, the potential crack is already considered in equation (41). To become a definitive crack, $\Delta\varepsilon_n^{cr}$ of the potential crack must be positive during the evaluation of equation (41). If this condition is not fulfilled, the crack initiation procedure is aborted and the tensile strength is replaced with the value of the current maximum principal stress.

After the determination of the transition point corresponding to the first critical crack status change (step 7), the stress vector is calculated, and the historical data of the cracks and the incremental strain vector are updated. The decomposition of the incremental strain vector ends when no more critical crack status changes occur (see Figure 9).

In this section, m is the counter of critical crack status changes, requiring a decomposition of the vector $\Delta\underline{\varepsilon}$. In Table 2 the meaning of "previous iteration" $m-1$ is clarified.

Table 2 – Meaning of $m-1$ value.

m **value**	**Algorithmic strategy (PD or PI)**	**Meaning of** $m-1$
$m=0$	Path dependent	Previous Newton-Raphson iteration
	Path independent	Previous converged combination
$m>0$	Path dependent or path independent	Previous iteration in the algorithm of Figure 9

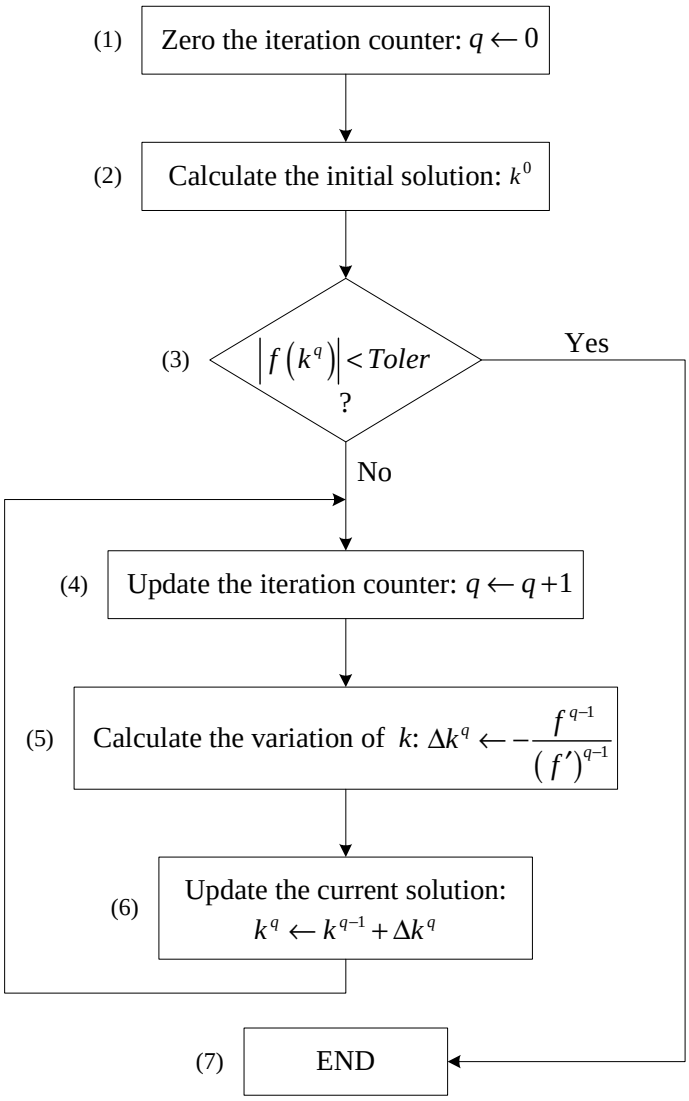

Figure 10 – Calculation of the transition point by the Newton-Raphson method.

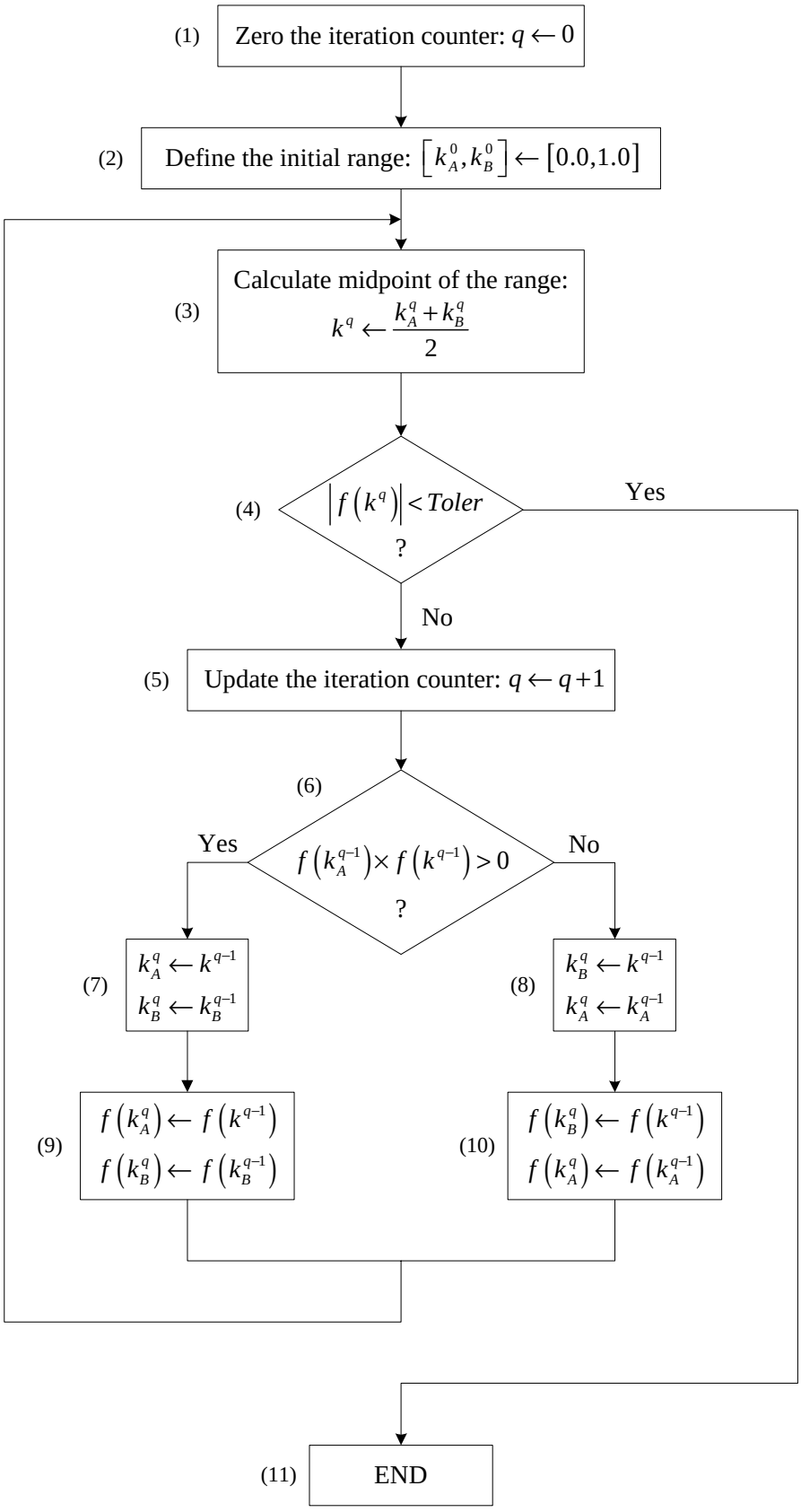

Figure 11 – Calculation of the transition point by the bisection method.

2.3.3 Singularities

When two fully open orthogonal cracks occur at an integration point, it can be shown that, in the system of nonlinear equations (41), the shear equations related to these cracks are linear dependent. This situation can be illustrated with the following example.

Considering two orthogonal cracks, being one horizontal ($\theta_1 = 90^o$) and the other vertical ($\theta_2 = 0^o$), and considering that both are fully open, the variation of the crack stress vector, $\Delta\underline{\sigma}_{\ell}^{cr}$, is null. Assuming that in the previous state $\underline{\sigma}_{\ell,m-1}^{cr} = \underline{T}_m^{cr}\underline{\sigma}_{m-1}$, equation (41) leads to

$$\underline{T}_m^{cr}\underline{D}^{co}\left[\underline{T}_m^{cr}\right]^T \Delta\underline{\varepsilon}_{\ell,m}^{cr} - \underline{T}_m^{cr}\underline{D}^{co}\Delta\underline{\varepsilon}_m = \underline{0} \tag{47}$$

resulting in

$$\begin{cases} \Delta\varepsilon_n^{cr,1} = \Delta\varepsilon_2 \\ +\Delta\gamma_t^{cr,1} - \Delta\gamma_t^{cr,2} = -\Delta\gamma_{12} \\ \Delta\varepsilon_n^{cr,2} = \Delta\varepsilon_1 \\ -\Delta\gamma_t^{cr,1} + \Delta\gamma_t^{cr,2} = +\Delta\gamma_{12} \end{cases} \tag{48}$$

where $\Delta\varepsilon_n^{cr,1}$, $\Delta\gamma_t^{cr,1}$, $\Delta\varepsilon_n^{cr,2}$ and $\Delta\gamma_t^{cr,2}$ are the normal and shear crack strain variations of the crack 1 and 2, respectively. The system of equations (48) cannot be solved since the second and fourth equations are linearly dependent. A physical interpretation of this situation is presented in Figure 12. The crack normal strain variations can be obtained directly from the global strain variations.

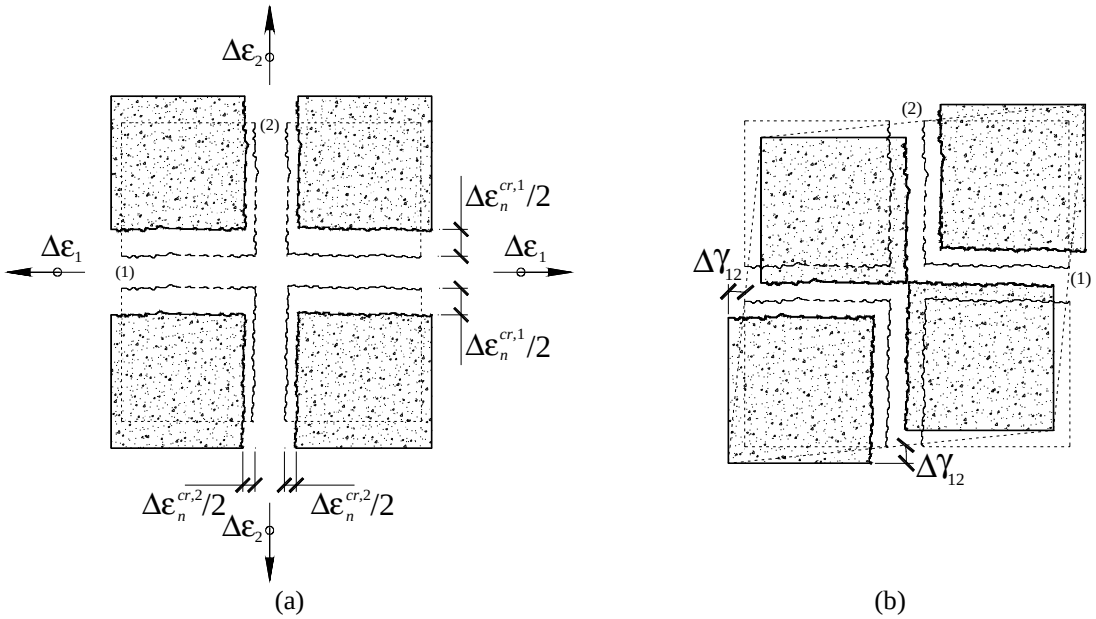

Figure 12 – Crack strain variation: (a) normal strain and (b) shear component.

The solution of (41) for the case of fully open orthogonal cracks requires the introduction of the following additional condition

$$\Delta\gamma_t^{cr,i} + \Delta\gamma_t^{cr,j} = 0 \tag{49}$$

where $\Delta\gamma_t^{cr,i}$ and $\Delta\gamma_t^{cr,j}$ are the crack shear strains variations of a pair orthogonal cracks.

To calculate the stiffness matrix of an element, $\underline{K}$, the constitutive matrix, $\underline{D}$, is required. The calculation of $\underline{D}$ of a cracked concrete integration point requires the inversion of the matrix that results from the evaluation of the following expression (see section 2.1.4, equation (18))

$$\underline{D}' = \underline{D}^{cr} + \underline{T}^{cr}\underline{D}^{co}\left[\underline{T}^{cr}\right]^T \tag{50}$$

When an integration point has two fully open orthogonal cracks, $\underline{D}^{cr}$ is null resulting in a singular $\underline{D}'$ matrix. To overcome this problem the following residual value is assigned to $\underline{D}^{cr}$,

$$D_{II}^{cr} = 10^{-6} G_c \tag{51}$$

2.4 Model appraisal

The performance of the developed multi-fixed smeared crack model is assessed using results published by other researchers. Since the concrete plastic deformation is not considered in the formulation described, the example selected to validate the model exhibit a linear behavior in compression.

Three-point bending tests are commonly used to evaluate the concrete tensile strength and the fracture energy (RILEM 1985). The tests carried out by Kormeling and Reihnardt (1983) are simulated using the implemented numerical model. The adopted mesh (see Figure 13) was composed of 4-node Lagrangian plane stress elements with 2×2 Gauss-Legendre integration scheme. In order to obtain a well-defined crack pattern at mid-span, ahead the notch, 1×2 Gauss-Legendre integration rule was used in the elements cross the center line.

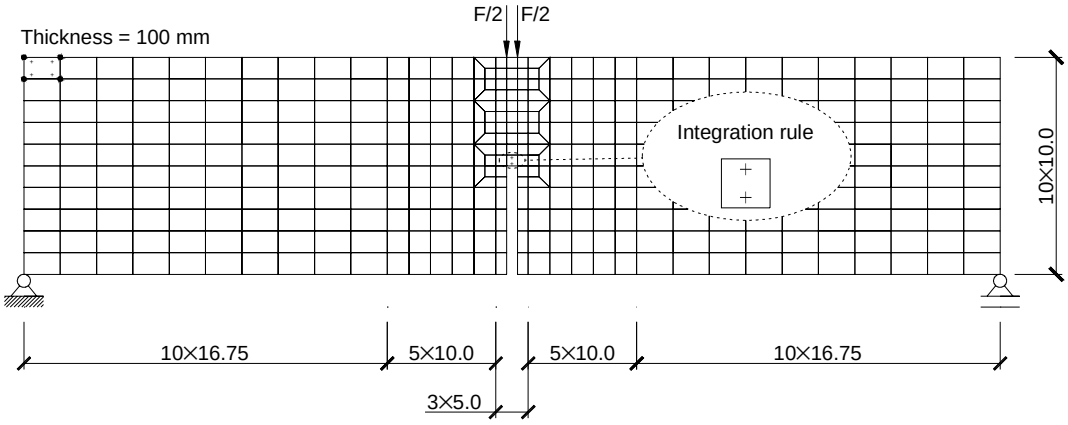

Figure 13 – Notched beam: geometry, mesh, loading configuration and support conditions. Note: all dimensions are in millimeters.

The concrete properties used in the present simulation are listed in Table 3. Three different types of tensile-softening diagrams were used: linear, tri-linear and exponential. The beam weight was included in the simulation.

Figure 14 presents the response obtained using the three different types of tensile-softening diagrams described above. The experimental results are also displayed. It can be observed that all numerical simulations have the same pre-peak response, up to 1050 kN. The maximum numerical peak load was obtained with the linear softening diagram. The

tri-linear and the exponential tensile-softening diagrams lead to an identical response in the post-peak phase, in good agreement with the experimental results.

Figure 15 shows the crack pattern at the final stage, for the case of tri-linear diagram. A well-defined crack above the notch can be observed. Spurious cracks with *closing* status were formed in the neighborhood of the fracture surface.

Table 3 – Concrete properties used in the simulation of the three point bending test.

Density	$\rho = 2.4\times10^{-6}$ N/mm^3
Poisson's ratio	$\nu_c = 0.20$
Initial Young's modulus	$E_c = 20000.0$ N/mm^2
Compression strength	$f_c = 48.0$ N/mm^2
Tensile strength	$f_{ct} = 2.4$ N/mm^2
Tri-linear softening parameters	$\xi_1 = 0.4$; $\alpha_1 = 0.6$; $\xi_2 = 0.8$; $\alpha_2 = 0.2$
Fracture energy	$G_f = 0.113$ N/mm
Parameter defining the mode I fracture energy available to the new crack	$p_1 = 2$
Shear retention factor	*Exponential* ($p_2 = 2$)
Crack band-width	*Square root of the area of the element*
Threshold angle	$\alpha_{th} = 30^o$

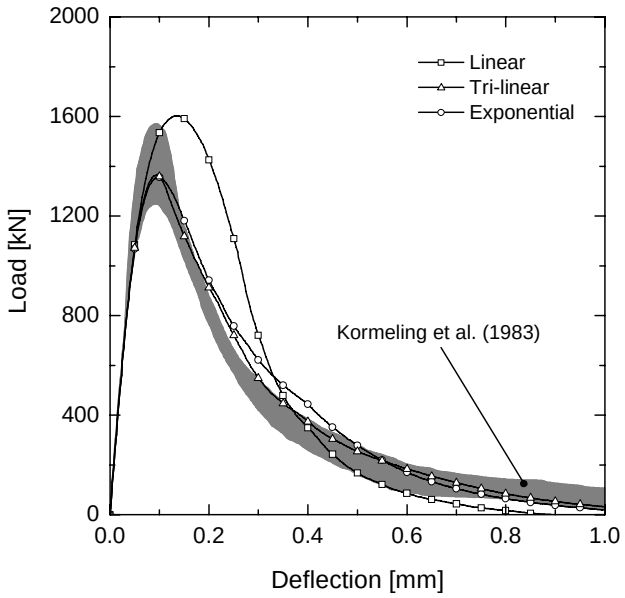

Figure 14 – Influence of the type of tensile-softening diagram on the load-deflection response.

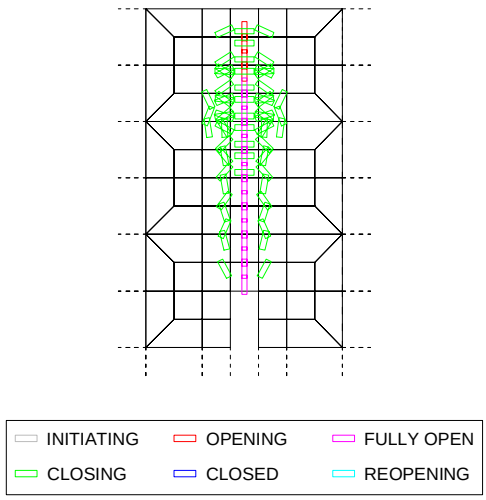

Figure 15 – Numerical crack pattern at the final stage using the tri-linear diagram.

3 PLASTICITY

The plasticity theory has been used by many researchers in the simulation of the behavior of structures built with materials exhibiting irreversible deformations, such as concrete (Chen 1982), soils (Chen and Mizuno 1990) or masonry (Lourenço 1996). An extensive study of this subject can be found in the literature (Lemaitre anb Caboche 1985, Lubliner 1990, Crisfield 1997, Simo and Hughes 1998). In the simulation of compressed concrete, a model based on the plasticity theory is adopted. This model is described in the following sections. Results available in the literature are used to assess the performance of the model.

3.1 Basic assumptions

The basic assumption of the plasticity theory, in the context of small strains, is the decomposition of the incremental strain, $\Delta\underline{\varepsilon}$, in an elastic reversible part, $\Delta\underline{\varepsilon}^e$, and an irreversible or plastic part, $\Delta\underline{\varepsilon}^p$:

$$\Delta\underline{\varepsilon} = \Delta\underline{\varepsilon}^e + \Delta\underline{\varepsilon}^p \tag{52}$$

The elastic constitutive matrix, $\underline{D}^e$, is used to obtain the incremental stress vector, $\Delta\underline{\sigma}$,

$$\Delta\underline{\sigma} = \underline{D}^e \ \Delta\underline{\varepsilon}^e = \underline{D}^e \left(\Delta\underline{\varepsilon} - \Delta\underline{\varepsilon}^p\right) \tag{53}$$

Plasticity based models depend on the concepts of yield surface, flow rule and hardening (or softening) law. The yield surface, defined in stress space, limits the elastic behavior domain. In general, this surface is a function of the stress state in a point, $\underline{\sigma}$, and of some internal variables, $\underline{a}$ and κ, that define the evolution of the yield surface. The general equation of the yield surface is

$$f\left(\underline{\sigma}, \underline{a}, \kappa\right) = 0 \tag{54}$$

The back-stress vector, $\underline{a}$, locates the origin of the yield surface and κ is the scalar hardening parameter, which defines the amount of hardening or softening.

Depending on the evolution of the yield surface during the loading process, three basic hardening types can be defined (see Figure 16): isotropic hardening (Odqvist 1933), kinematic hardening (Prager 1955) and mixed hardening (Hodge 1957). The internal variables involved in these hardening rules are indicated in Table 4.

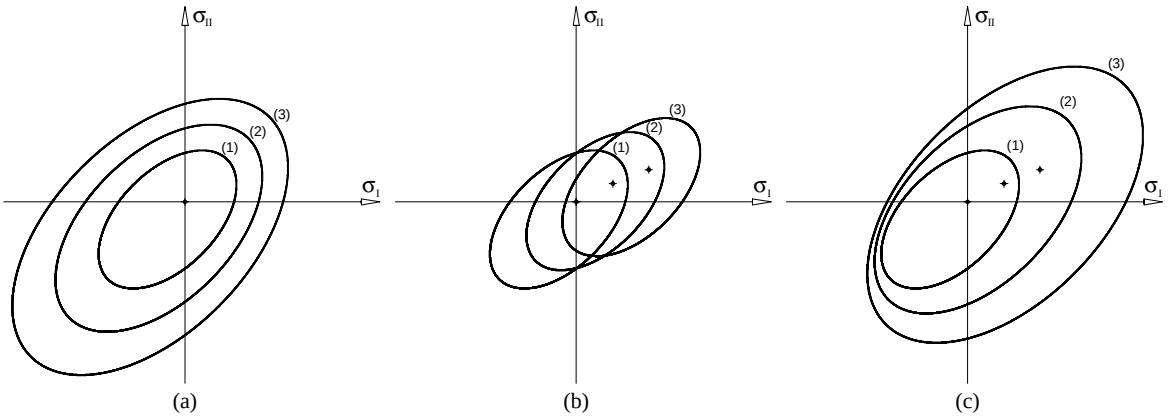

Figure 16 – Basic hardening rules: (a) isotropic hardening, (b) kinematic hardening and (c) mixed hardening.

Table 4 – Basic hardening rules.

Hardening rule	**Variables involved**
No hardening (ideal plasticity)	$f(\underline{\sigma})$
Isotropic hardening (Figure 16(a))	$f(\underline{\sigma},\kappa)$
Kinematic hardening (Figure 16(b))	$f(\underline{\sigma},\underline{a})$
Mixed hardening (Figure 16(c))	$f(\underline{\sigma},\underline{a},\kappa)$

In the geometric representation shown in Figure 16 $\underline{a}$ defines the location of the origin of the yield surface whereas κ controls the size and shape of the yield surface. Good results can be obtained with the isotropic hardening when loading is monotonic. However, more complex hardening rules are required when the material is submitted to cyclic loading. Since the aim of the present model is to simulate the behavior of concrete structures under monotonic loading, the back-stress vector will not be considered as a yield surface parameter. With these assumptions the yield condition adopted for the present model is the following

$$f(\underline{\sigma},\kappa)=0 \tag{55}$$

The evolution of the plastic strain is given by the following flow rule

$$\Delta\underline{\varepsilon}^{p}=\Delta\lambda\frac{\partial g}{\partial\underline{\sigma}} \tag{56}$$

where $\Delta\lambda$ is a non-negative scalar designated by plastic multiplier and g is the plastic potential function in stress space. When g and f coincide, the flow rule is named associated. Otherwise, a non-associated flow rule is obtained. The yield function and the plastic multiplier are constrained by the following conditions

$$f\le 0,\ \Delta\lambda\ge 0 \text{ and } \Delta\lambda f=0 \tag{57}$$

The variation of the hardening parameter, $\Delta\kappa$, coincides with the equivalent plastic strain variation $\Delta\varepsilon^{eps}$ (strain hardening) or with the plastic work variation ΔW^{p} (work

hardening). When the first hypothesis holds ($\Delta\kappa = \Delta\varepsilon^{eps}$), the hardening parameter is defined by

$$\Delta\kappa = \Delta\varepsilon^{eps} = c\sqrt{\left(\Delta\underline{\varepsilon}^{p}\right)^{T}\Delta\underline{\varepsilon}^{p}} \tag{58}$$

The assumption of $c = \sqrt{2/3}$ assures that the plastic strain in the loading direction of an uniaxial test is equal to the equivalent plastic strain variation, i.e., $\Delta\varepsilon^{eps} = \Delta\varepsilon_1^p$ and $\Delta\varepsilon_2^p = \Delta\varepsilon_3^p = -\Delta\varepsilon_1^p/2$ (Owen and Hinton 1980).

The equivalent plastic strain variation can also be defined as a function of the plastic work per unit volume, ΔW^p, resulting

$$\Delta\kappa = \Delta\varepsilon^{eps} = \frac{\Delta W^p}{\bar{\sigma}} = \frac{1}{\bar{\sigma}}\underline{\sigma}^{T}\Delta\underline{\varepsilon}^{p} \tag{59}$$

where $\bar{\sigma}$ is the uniaxial yield stress which depends on the hardening parameter, and is currently named hardening law. When the variation of the hardening parameter is defined with the work hardening hypotheses ($\Delta\kappa = \Delta W^p$), the following relation holds

$$\Delta\kappa = \Delta W^p = \underline{\sigma}^{T}\Delta\underline{\varepsilon}^{p} \tag{60}$$

3.2 Integration of the elasto-plastic constitutive equations

The integration of the elasto-plastic constitutive equations over a finite step in a consistent manner is one of the main challenges in computational plasticity. At the previous step $n-1$, the stress state and the internal variables are known ($\underline{\sigma}_{n-1}$, κ_{n-1}, $\underline{\varepsilon}_{n-1}$, $\underline{\varepsilon}_{n-1}^{p}$), and the main task is the calculation of the current values of these variables when a strain variation occurs, $\Delta\underline{\varepsilon}_n$. This problem can be solved with an implicit Euler backward integration algorithm. The stability and accuracy of this algorithm has been demonstrated by several researchers (Ortiz and Popov 1985, de Borst and Feenstra 1990, Schellekens and de Borst 1990). The algorithm has two phases: an elastic predictor phase and a plastic

corrector phase. In the former null plastic flow is assumed which leads to a discrete set of equations

$$\begin{cases} \underline{\sigma}_n = \underline{\sigma}_{n-1} + \underline{D}^e \Delta \underline{\varepsilon}_n \\ \kappa_n = \kappa_{n-1} \\ f_n = f\left(\underline{\sigma}_n, \kappa_n\right) = 0 \end{cases} \tag{61}$$

When the elastic trial stress, $\underline{\sigma}_n$, lies out the yield surface, plastic flow must be considered and the plastic corrector phase of the algorithm is used to find an admissible stress state. Otherwise, the load step is considered linear elastic. The algorithm used to find an admissible stress state is named return-mapping algorithm and consists in the solution of the following system of nonlinear equations,

$$\begin{cases} \left[\underline{D}^e\right]^{-1}\left(\underline{\sigma}_n - \underline{\sigma}_n^e\right) + \Delta\lambda_n \left(\dfrac{\partial g}{\partial \underline{\sigma}}\right)_n = \underline{0} \\ \kappa_n - \kappa_{n-1} - \Delta\kappa_n = 0 \\ f_n\left(\underline{\sigma}_n, \kappa_n\right) = 0 \end{cases} \tag{62}$$

The first equation of the system of nonlinear equations is obtained from the equation

$$\underline{\sigma}_n = \underline{\sigma}_{n-1} + \underline{D}^e\left(\Delta\underline{\varepsilon}_n - \Delta\underline{\varepsilon}_n^p\right) = \underline{\sigma}_n^e - \underline{D}^e \Delta\underline{\varepsilon}_n^p \tag{63}$$

where $\Delta\underline{\varepsilon}_n^p$ is replaced with the right-hand side of equation (56). The Newton-Raphson method is used to solve the system of nonlinear equations (62), where $\underline{\sigma}_n$, κ_n and $\Delta\lambda_n$ are the unknowns.

3.3 Evaluation of the tangent operator

In the present work, the Newton-Raphson method is used to calculate the solution of the system of nonlinear equations resulting from the nonlinear finite element analysis. The nonlinear problem is converted into a sequence of linear iterations until convergence is

reached. The linearized form of the equations depends on a tangent stiffness matrix, $\underline{K}_T$, which plays a crucial role in the performance and robustness of the Newton-Raphson method. In the context of the mathematical plasticity, and according to Simo and Taylor (1985), the tangent stiffness matrix must be obtained by consistent linearization of the stress update resulting from the return-mapping algorithm at the end of the iteration i.

The elasto-plastic consistent tangent constitutive matrix can be determined from the total differentials $d\underline{\sigma}_n$, $d\underline{\varepsilon}_n^p$ and df_n (Hofstetter and Mang 1995) or from part of the Jacobian matrix used in the Newton-Raphson method of the return-mapping algorithm (Lourenço 1996).

3.4 Elasto-plastic concrete model

Several elasto-plastic models have been proposed to simulate the concrete behavior. These models differ from each other, mainly, in the shape of the yield surface and in the hardening and flow rules. The model described in this section is suitable to simulate the concrete compressive behavior under monotonic loading, admitting that the tensile stresses do not exceed the concrete tensile strength.

3.4.1 Yield surface

The yield surface proposed by Owen and Figueiras (1983) was adopted in the present model. Its main characteristic is the consideration of parabolic meridians. This yield surface is defined with the following equation

$$f\left(\underline{\sigma},\kappa\right)=\left(\underline{\sigma}^T\underline{P}\underline{\sigma}\right)^{1/2}+\underline{q}^T\underline{\sigma}-\bar{\sigma}\left(\kappa\right)=0 \tag{64}$$

where $\underline{P}$ is the projection matrix, given by

$$\underline{P}=\begin{bmatrix} a & b & 0 \\ b & a & 0 \\ 0 & 0 & c \end{bmatrix} \tag{65}$$

and $\underline{q}$ is the projection vector defined by

$$\underline{q} = d\underline{q}_1 = d\begin{bmatrix}1 & 1 & 0\end{bmatrix}^T \tag{66}$$

The parameters a, b, c and d can be obtained with

$$a = \left(\frac{A}{2}\right)^2 + B,\ b = \left(\frac{A}{2}\right)^2 - \frac{B}{2},\ c = 3B,\ d = \frac{A}{2} \tag{67}$$

where the scalars A and B assume the values that result from the fitting process between the present model and the experimental results obtained by Kupfer et al. (1969). In these circumstances, A and B assumes the values of (Owen and Figueiras 1983)

$$A = 0.355 \text{ and } B = 1.355 \tag{68}$$

Figure 17 represents the initial and the limit yield surfaces. This initial yield surface is the limiting surface for elastic behavior. Experimental results obtained by Kupfer et al. (1969) are also included.

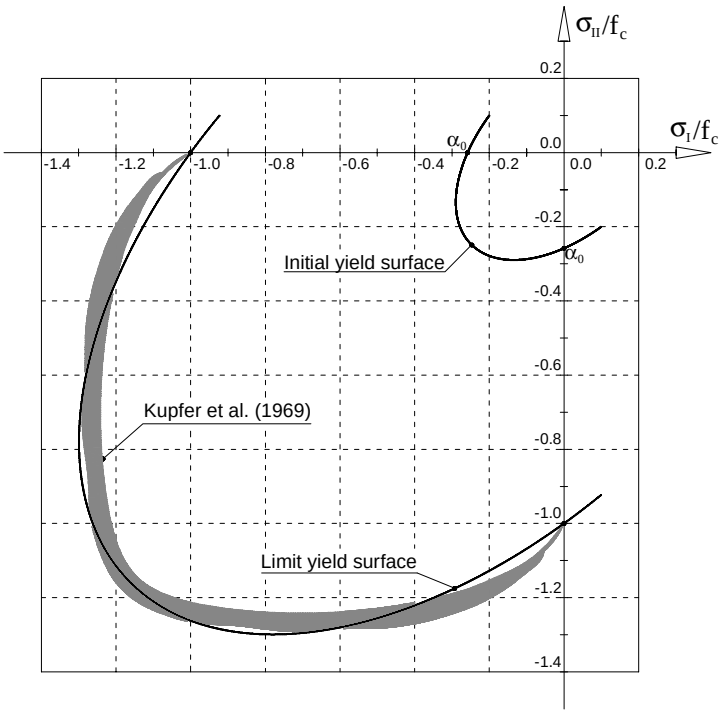

Figure 17 – Yield surface for concrete.

3.4.2 Hardening behavior

Figure 18 represents the relationship between the yield stress, $\bar{\sigma}$, and the hardening parameter, κ, used to simulate the hardening and softening phases of the concrete behavior. Three points define the transitions between the branches of the curve. The location of these points is obtained from uniaxial compression tests: $\bar{\sigma}_0 = \alpha_0 f_c$, $\bar{\sigma}_p = f_c$ and $\bar{\sigma}_{\text{lim}} = 0.5 f_c$. The equivalent plastic strain corresponding to the peak compressive strength, κ_p, with the following equation,

$$\kappa_p = \varepsilon_{c1} - f_c / E_c \tag{69}$$

where ε_{c1} is the total strain at the peak compressive strength. The α_0 parameter defines the beginning of the plastic behavior. In most cases α_0 can assume the value 0.3.

For the hardening branch, $\bar{\sigma}_1(\kappa)$, the relationship used by Lourenço (1996) was adopted, whereas for the softening phase, $\bar{\sigma}_2(\kappa)$ and $\bar{\sigma}_3(\kappa)$, the post-peak relationship proposed by CEB-FIB (1993) for the uniaxial compressive behavior was used. The expressions of the hardening (and softening) behavior laws are included in APPENDIX I.

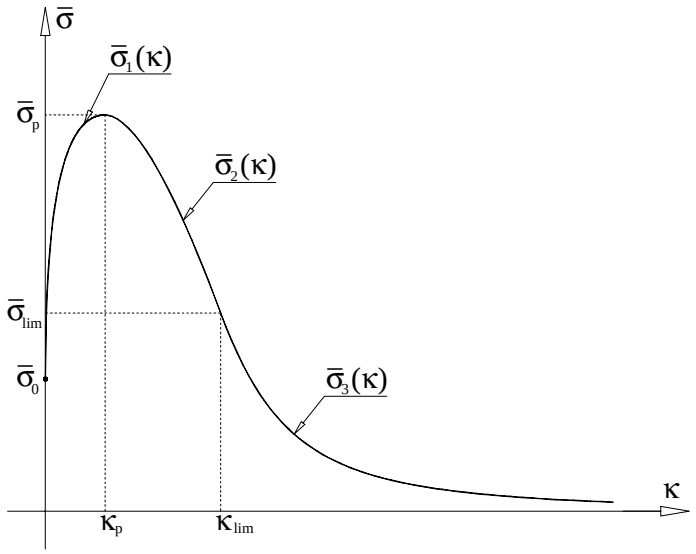

Figure 18 – Hardening/softening law for concrete.

The plastic strain variation is described by the following expression which is assumed to be valid when an associated flow rule is considered

$$\Delta \underline{\varepsilon}^{p} = \Delta\lambda \frac{\partial g}{\partial \underline{\sigma}} = \Delta\lambda h_c \frac{\partial f}{\partial \underline{\sigma}} \tag{70}$$

The scalar function h_c is included in this equation in order to amplify the contribution of $\Delta\lambda \partial f / \partial \underline{\sigma}$ to $\Delta \underline{\varepsilon}^{p}$. The function h_c depends on the hydrostatic pressure, *p*, and reads (Abaqus 2002)

$$h_c = h_c\left(\underline{\sigma}\right) = 1 + c_0 \left(\frac{p}{f_c} \right)^2 \tag{71}$$

A value of 6.056 for c_0 was obtained based on the condition that under biaxial compression, with equal compressive stress in both directions, the plastic strain at failure is, according to Kupfer et al. (1969), approximately 1.28 times the plastic strain at failure under uniaxial compression.

3.4.3 Return-mapping algorithm

Assuming the strain-hardening hypothesis, $\Delta\kappa = \Delta\lambda$ (Cachim 1999, Abaqus 2002), the system of nonlinear equations (62) can be reduced to the following pair of equations,

$$\begin{cases} \underline{f}_{1,n} = \left[\underline{D}^{e} \right]^{-1} \left(\underline{\sigma}_n - \underline{\sigma}_n^{e} \right) + \Delta\kappa_n h_{c,n} \left(\dfrac{\partial f}{\partial \underline{\sigma}} \right)_n = \underline{0} \\ f_{2,n} = f\left(\underline{\sigma}_n, \kappa_n \right) = 0 \end{cases} \tag{72}$$

Figure 19 shows the return-mapping algorithm currently implemented in the computer code. The norm defined in step (4) is given by

$$\left\| \underline{r}_n^q \right\| = \begin{bmatrix} \left\| \left[D^e \right]^{-1} \left(\underline{\sigma}_n^q - \underline{\sigma}_n^e \right) + \Delta\kappa_n^q h_{c,n}^q \left(\frac{\partial f}{\partial \underline{\sigma}} \right)_n^q \right\|_\infty \\ \left| f\left(\underline{\sigma}_n^q, \kappa_n^q \right) \right| \end{bmatrix} \tag{73}$$

where the superscript q corresponds to the iteration counter. The Jacobian matrix used in step (6) is defined by the following four blocks

$$\begin{aligned} \underline{J} &= \left[\begin{array}{c|c} \dfrac{\partial f_1}{\partial \underline{\sigma}} & \dfrac{\partial f_1}{\partial \kappa} \\ \hline \dfrac{\partial f_2}{\partial \underline{\sigma}} & \dfrac{\partial f_2}{\partial \kappa} \end{array} \right] \\ &= \left[\begin{array}{c|c} \left[\underline{D}^e \right]^{-1} + \Delta\kappa \left(\dfrac{\partial f}{\partial \underline{\sigma}} \left(\dfrac{\partial h_c}{\partial \underline{\sigma}} \right)^T + h_c \dfrac{\partial^2 f}{\partial \underline{\sigma}^2} \right) & h_c \dfrac{\partial f}{\partial \underline{\sigma}} \\ \hline \left(\dfrac{\partial f}{\partial \underline{\sigma}} \right)^T & \dfrac{\partial f}{\partial \kappa} \end{array} \right] \end{aligned} \tag{74}$$

where

$$\begin{aligned} &\frac{\partial f}{\partial \underline{\sigma}} = \frac{\underline{P}\underline{\sigma}}{\left(\underline{\sigma}^T \underline{P} \underline{\sigma} \right)^{1/2}} + \underline{q}\,; \qquad && \frac{\partial^2 f}{\partial \underline{\sigma}^2} = \frac{\underline{P}\underline{\sigma}}{\left(\underline{\sigma}^T \underline{P} \underline{\sigma} \right)^{1/2}} - \frac{\underline{P}\underline{\sigma}\underline{\sigma}^T \underline{P}}{\left(\underline{\sigma}^T \underline{P} \underline{\sigma} \right)^{3/2}} \\ &\frac{\partial h_c}{\partial \underline{\sigma}} = 2c_0 \frac{p}{f_c^2} \underline{q}_1\,; && \frac{\partial f}{\partial \kappa} = -\frac{d\bar{\sigma}}{d\kappa} = -h \end{aligned} \tag{75}$$

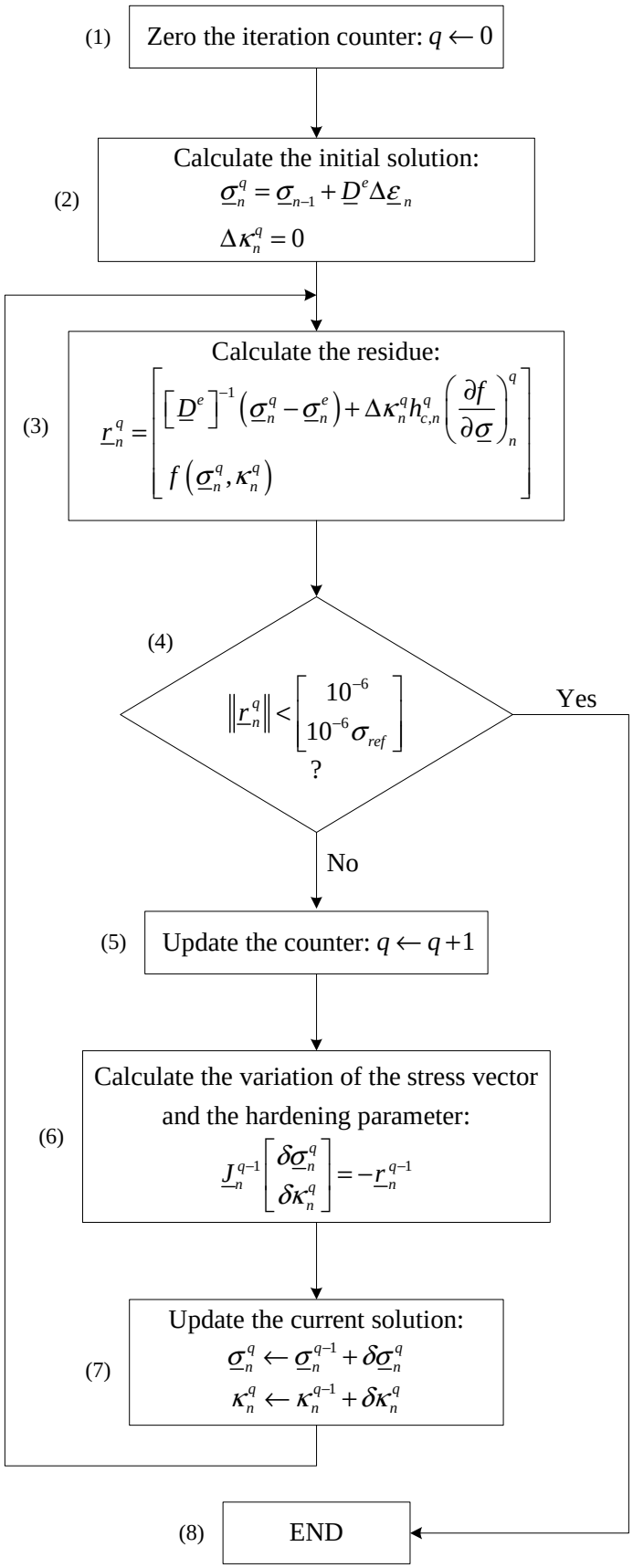

Figure 19 – Return-mapping algorithm of the elasto-plastic model.

3.4.4 Consistent tangent constitutive matrix

The consistent tangent constitutive matrix adopted in the present numerical model is deduced in APPENDIX II, resulting

$$\underline{D}^{ep} = \underline{H} - \frac{\underline{H}\dfrac{\partial f}{\partial \underline{\sigma}}\left(\dfrac{\partial f}{\partial \underline{\sigma}}\right)^{T}\underline{H}}{h + \left(\dfrac{\partial f}{\partial \underline{\sigma}}\right)^{T}\underline{H}\dfrac{\partial f}{\partial \underline{\sigma}}} \tag{76}$$

where

$$\underline{H} = \left(\left[D^{e}\right]^{-1} + h_{c}\Delta\lambda\frac{\partial^{2} f}{\partial \underline{\sigma}^{2}}\right)^{-1} \tag{77}$$

3.5 Model appraisal

The performance and the accuracy of the developed elasto-plastic model are assessed using results available from the literature. All the selected examples are governed by the compressive behavior.

3.5.1 Uniaxial compressive tests

The uniaxial compressive tests 3B2-4 to 3B2-6, carried out by Van Mier (1984), were selected for a comparison with the proposed model. One single 4-node Lagrangian plane stress finite element with 1×1 Gauss-Legendre integration scheme was used to simulate the experimental results. The dimensions of the finite element coincides with those of specimen (200×200×200 mm^3). Table 5 shows the adopted concrete properties. The numerical and the experimental results are compared in Figure 20.

Table 5 – Concrete properties used in the simulation of the uniaxial compressive test.

Poisson's ratio	$\nu_c = 0.20$
Initial Young's modulus	$E_c = 33344.0$ N/mm^2
Compression strength	$f_c = 43.24$ N/mm^2
Strain at peak compression stress	$\varepsilon_{c1} = 2.7\times10^{-3}$
Parameter defining the initial yield surface	$\alpha_0 = 0.3$

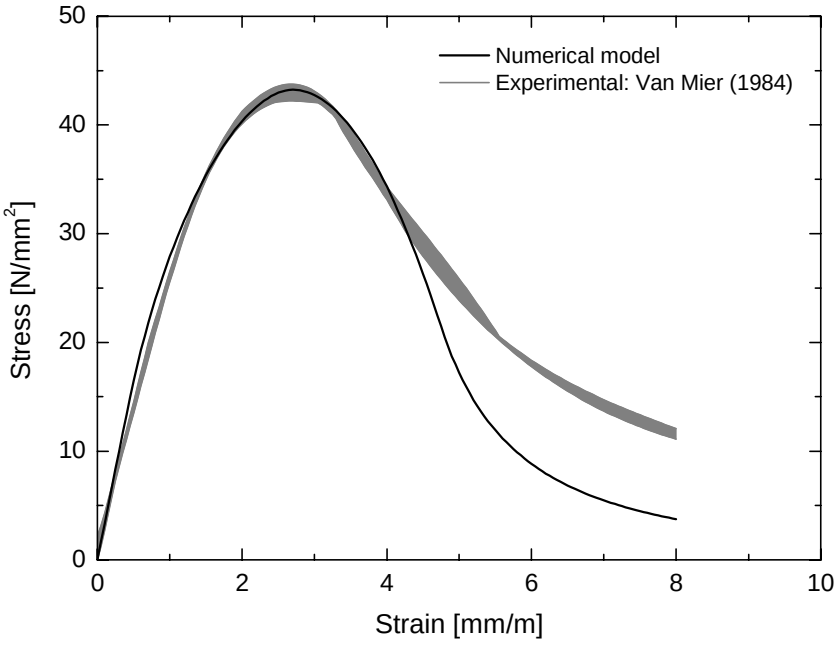

Figure 20 – Stress-strain relationships: experimental and numerical results.

Up to peak stress, the model matches with high accuracy the experimental results. In the softening phase, and for strains higher than 4.5 ‰, the model estimates a residual strength that is lower than those experimentally obtained. This indicates that the softening branch of the uniaxial compressive behavior proposed by CEB-FIB (1993), mainly the second softening branch, $\bar{\sigma}_3(\kappa)$, may not be suitable to reproduce this type of test.

3.5.2 Biaxial compressive test

To evaluate the importance of the h_c parameter in the flow rule, the biaxial compressive tests carried out by Kupfer et al. (1969) were selected. One single 4-node Lagrangian plane stress element with 1×1 Gauss-Legendre integration scheme was used in the numerical

model. Table 6 shows the properties adopted for the concrete and for the yield surface. In Figure 21 the numerical simulation with $c_0 = 0$ ($h_c = 1.0$) and $c_0 = 6.056$ are compared with the experimental results.

Table 6 – Concrete properties used in the simulation of the biaxial compressive test.

Poisson's ratio	$\nu_c = 0.20$
Initial Young's modulus	$E_c = 30180.0$ N/mm^2
Compression strength	$f_c = 32.06$ N/mm^2
Strain at peak compression stress	$\varepsilon_{c1} = 2.2\times10^{-3}$
Parameter defining the initial yield surface	$\alpha_0 = 0.3$

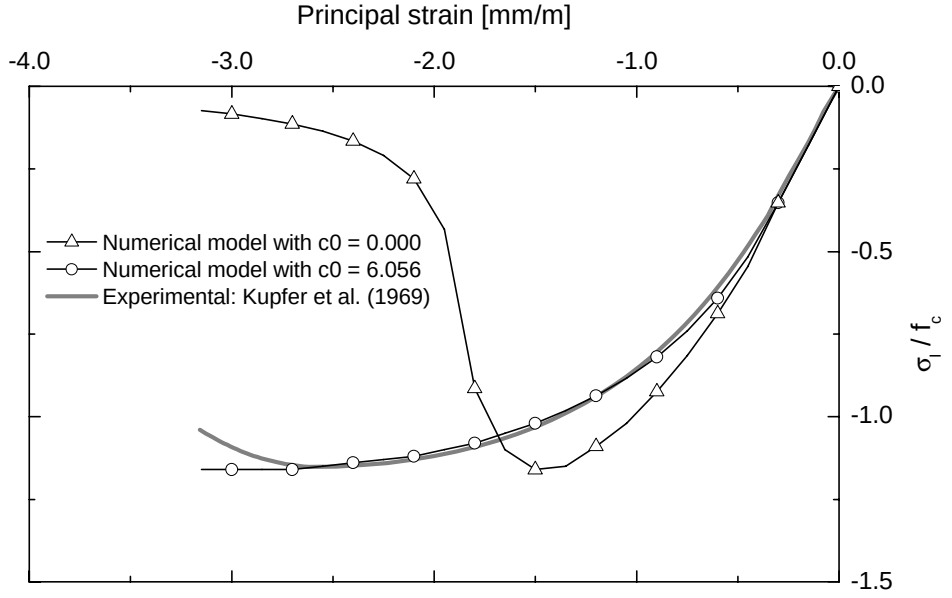

Figure 21 – Influence of the c_0 parameter in numerical response.

The results shown in the Figure 21 indicate that the response obtained with $c_0 = 0$ is stiffer in the hardening phase and too brittle after the peak stress. A good agreement with the experimental results was obtained with $c_0 = 6.056$.

4 ELASTO-PLASTIC MULTI-FIXED SMEARED CRACK MODEL

In the present section an elasto-plastic multi-fixed smeared crack model is proposed. This model corresponds to the coupling of the multi-fixed smeared crack model described in Section 2 and the elasto-plastic model presented in Section 3. In the following sections the implemented model is described.

4.1 Yield surface

Two types of yield surface were combined in the proposed numerical model: the Rankine criterion (described in Section 2) for concrete in tension, and the Owen and Figueiras (1983) yield surface (described in Section 3) for concrete in compression. Figure 22 represents the initial and the limit yield surfaces. Experimental results from Kupfer et al. (1969) are also included.

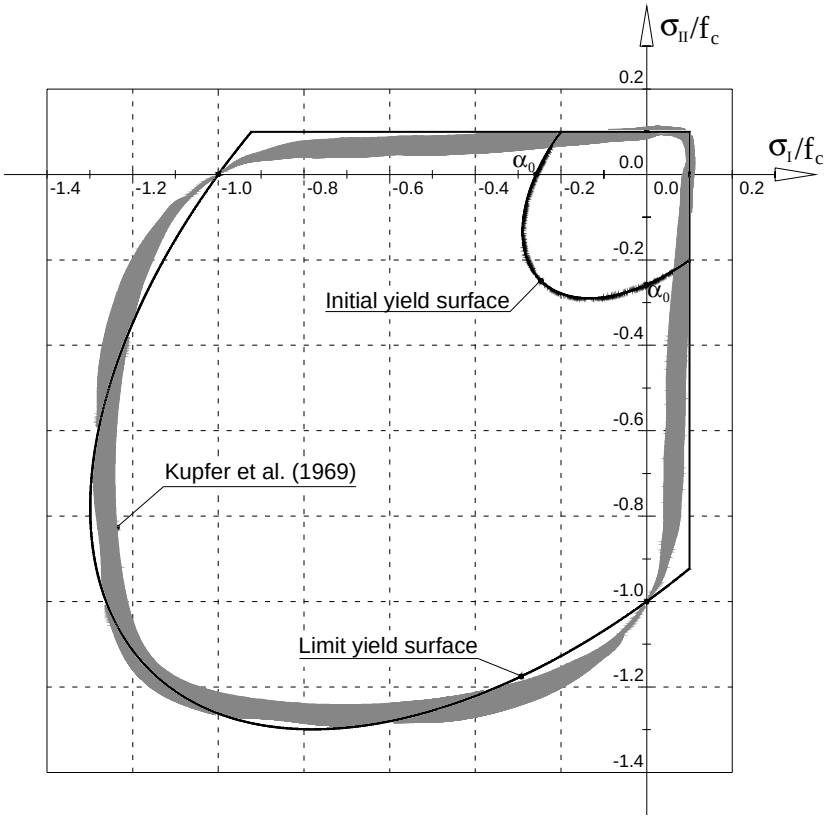

Figure 22 – Yield surfaces adopted in the elasto-plastic multi-fixed smeared crack model.

4.2 Integration of the constitutive equations

The incremental strain vector is decomposed in an incremental crack strain vector, $\Delta\underline{\varepsilon}^{cr}$, and an incremental strain vector of the concrete between cracks, $\Delta\underline{\varepsilon}^{co}$. This vector is decomposed in an elastic reversible part, $\Delta\underline{\varepsilon}^{e}$, and an irreversible or plastic part, $\Delta\underline{\varepsilon}^{p}$, resulting

$$\Delta\underline{\varepsilon} = \Delta\underline{\varepsilon}^{cr} + \Delta\underline{\varepsilon}^{co} = \Delta\underline{\varepsilon}^{cr} + \Delta\underline{\varepsilon}^{e} + \Delta\underline{\varepsilon}^{p} \tag{78}$$

The constitutive equations of the present model follow the multi-fixed smeared crack model and the elasto-plastic model and are deduced in the following sections.

4.2.1 Constitutive equations from the multi-fixed smeared crack model

The incremental stress vector can be computed from the incremental elastic strain vector,

$$\Delta\underline{\sigma}_{m} = \underline{D}^{e}\Delta\underline{\varepsilon}_{m}^{e} \tag{79}$$

Incorporating (79) into (39) leads to

$$\underline{\sigma}_{\ell,m-1}^{cr} + \Delta\underline{\sigma}_{\ell,m}^{cr} = \underline{T}_{m}^{cr}\left(\underline{\sigma}_{m-1} + \underline{D}^{e}\Delta\underline{\varepsilon}_{m}^{e}\right) \tag{80}$$

Substituting (78) into (80) yields

$$\underline{\sigma}_{\ell,m-1}^{cr} + \Delta\underline{\sigma}_{\ell,m}^{cr} = \underline{T}_{m}^{cr}\underline{\sigma}_{m-1} + \underline{T}_{m}^{cr}\underline{D}^{e}\left(\Delta\underline{\varepsilon}_{m} - \Delta\underline{\varepsilon}_{m}^{p}\right) - \underline{T}_{m}^{cr}\underline{D}^{e}\left[\underline{T}_{m}^{cr}\right]^{T}\Delta\underline{\varepsilon}_{\ell,m}^{cr} \tag{81}$$

and including (70) in (81) results in

$$\begin{aligned}&\underline{\sigma}_{\ell,m-1}^{cr} + \Delta\underline{\sigma}_{\ell,m}^{cr}\left(\Delta\underline{\varepsilon}_{\ell,m}^{cr}\right) + \underline{T}_{m}^{cr}\underline{D}^{e}\left[\underline{T}_{m}^{cr}\right]^{T}\Delta\underline{\varepsilon}_{\ell,m}^{cr} - \underline{T}_{m}^{cr}\underline{\sigma}_{m-1} - \\ &\underline{T}_{m}^{cr}\underline{D}^{e}\left(\Delta\underline{\varepsilon}_{m} - \Delta\lambda_{m}h_{c,m}\left(\frac{\partial f}{\partial\underline{\sigma}}\right)_{m}\right) = \underline{0}\end{aligned} \tag{82}$$

4.2.2 Constitutive equations from the elasto-plastic model

The incremental elastic strain vector, $\Delta\underline{\varepsilon}_m^e$, multiplied by the elastic constitutive matrix, $\underline{D}^e$, is used to update the stress vector, which leads to

$$\underline{\sigma}_m = \underline{\sigma}_{m-1} + \underline{D}^e \Delta\underline{\varepsilon}_m^e \tag{83}$$

Including (78) and (70) in (83) yields to

$$\underline{\sigma}_m = \underline{\sigma}_{m-1} + \underline{D}^e \left(\Delta\underline{\varepsilon}_m - \Delta\underline{\varepsilon}_m^{cr}\right) - \Delta\lambda_m h_{c,m} \underline{D}^e \left(\frac{\partial f}{\partial \underline{\sigma}}\right)_m \tag{84}$$

This equation can be written in a more suitable format as

$$\left[\underline{D}^e\right]^{-1} \left(\underline{\sigma}_m - \underline{\sigma}_{m-1} - \underline{D}^e \left(\Delta\underline{\varepsilon}_m - \Delta\underline{\varepsilon}_m^{cr}\right)\right) + \Delta\lambda_m h_{c,m} \left(\frac{\partial f}{\partial \underline{\sigma}}\right)_m = \underline{0} \tag{85}$$

or

$$\left[\underline{D}^e\right]^{-1} \left(\underline{\sigma}_m - \underline{\sigma}_{m-1} - \underline{D}^e \left(\Delta\underline{\varepsilon}_m - \left[\underline{T}_m^{cr}\right]^T \Delta\underline{\varepsilon}_{l,m}^{cr}\right)\right) + \Delta\lambda_m h_{c,m} \left(\frac{\partial f}{\partial \underline{\sigma}}\right)_m = \underline{0} \tag{86}$$

4.2.3 Return-mapping algorithm

Equations (82), (86) and (64) define the system of nonlinear equations that corresponds to the return-mapping algorithm of the present model. Assuming $\Delta\kappa = \Delta\lambda$ (see Section 3.4.3) this system becomes

$$\begin{cases} \underline{f}_{1,m} = \underline{\sigma}^{cr}_{\ell,m-1} + \Delta\underline{\sigma}^{cr}_{\ell,m}\left(\Delta\underline{\varepsilon}^{cr}_{\ell,m}\right) + \underline{T}^{cr}_{m}\underline{D}^{e}\left[\underline{T}^{cr}_{m}\right]^{T}\Delta\underline{\varepsilon}^{cr}_{\ell,m} - \underline{T}^{cr}_{m}\underline{\sigma}_{m-1} - \\ \qquad \underline{T}^{cr}_{m}\underline{D}^{e}\left(\Delta\underline{\varepsilon}_{m} - \Delta\kappa_{m}h_{c,m}\left(\dfrac{\partial f}{\partial\underline{\sigma}}\right)_{m}\right) = \underline{0} \\ \underline{f}_{2,m} = \left[\underline{D}^{e}\right]^{-1}\left(\underline{\sigma}_{m} - \underline{\sigma}_{m-1} - \underline{D}^{e}\left(\Delta\underline{\varepsilon}_{m} - \left[\underline{T}^{cr}_{m}\right]^{T}\Delta\underline{\varepsilon}^{cr}_{\ell,m}\right)\right) + \Delta\kappa_{m}h_{c,m}\left(\dfrac{\partial f}{\partial\underline{\sigma}}\right)_{m} = \underline{0} \\ f_{3,m} = f\left(\underline{\sigma}_{m}, \kappa_{m}\right) = 0 \end{cases} \tag{87}$$

In the system of nonlinear equations (86) the unknowns are $\Delta\underline{\varepsilon}^{cr}_{\ell,m}$, $\underline{\sigma}_{m}$ and κ_{m}. Figure 23 shows the return-mapping algorithm implemented in the present computer code. The determination of the initial solution is based on the assumption of null plastic flow (see step 2). The residual vector defined in step (3) is given by

$$\underline{r}_{m} = \left[\begin{array}{ccc} \underline{f}_{1,m} & \underline{f}_{2,m} & f_{3,m} \end{array}\right]^{T} \tag{88}$$

and the corresponding norm (step 4) is defined as

$$\left\|\underline{r}_{m}\right\| = \left[\begin{array}{ccc} \left\|\underline{f}_{1,m}\right\|_{\infty} & \left\|\underline{f}_{2,m}\right\|_{\infty} & \left|f_{3,m}\right| \end{array}\right]^{T} \tag{89}$$

The Jacobian matrix of step (6) is composed of nine blocks

$$\underline{J} = \begin{bmatrix} \dfrac{\partial\underline{f}_{1}}{\partial\Delta\underline{\varepsilon}^{cr}_{\ell}} & \dfrac{\partial\underline{f}_{1}}{\partial\underline{\sigma}} & \dfrac{\partial\underline{f}_{1}}{\partial\kappa} \\ \dfrac{\partial\underline{f}_{2}}{\partial\Delta\underline{\varepsilon}^{cr}_{\ell}} & \dfrac{\partial\underline{f}_{2}}{\partial\underline{\sigma}} & \dfrac{\partial\underline{f}_{2}}{\partial\kappa} \\ \dfrac{\partial f_{3}}{\partial\Delta\underline{\varepsilon}^{cr}_{\ell}} & \dfrac{\partial f_{3}}{\partial\underline{\sigma}} & \dfrac{\partial f_{3}}{\partial\kappa} \end{bmatrix} \tag{90}$$

being

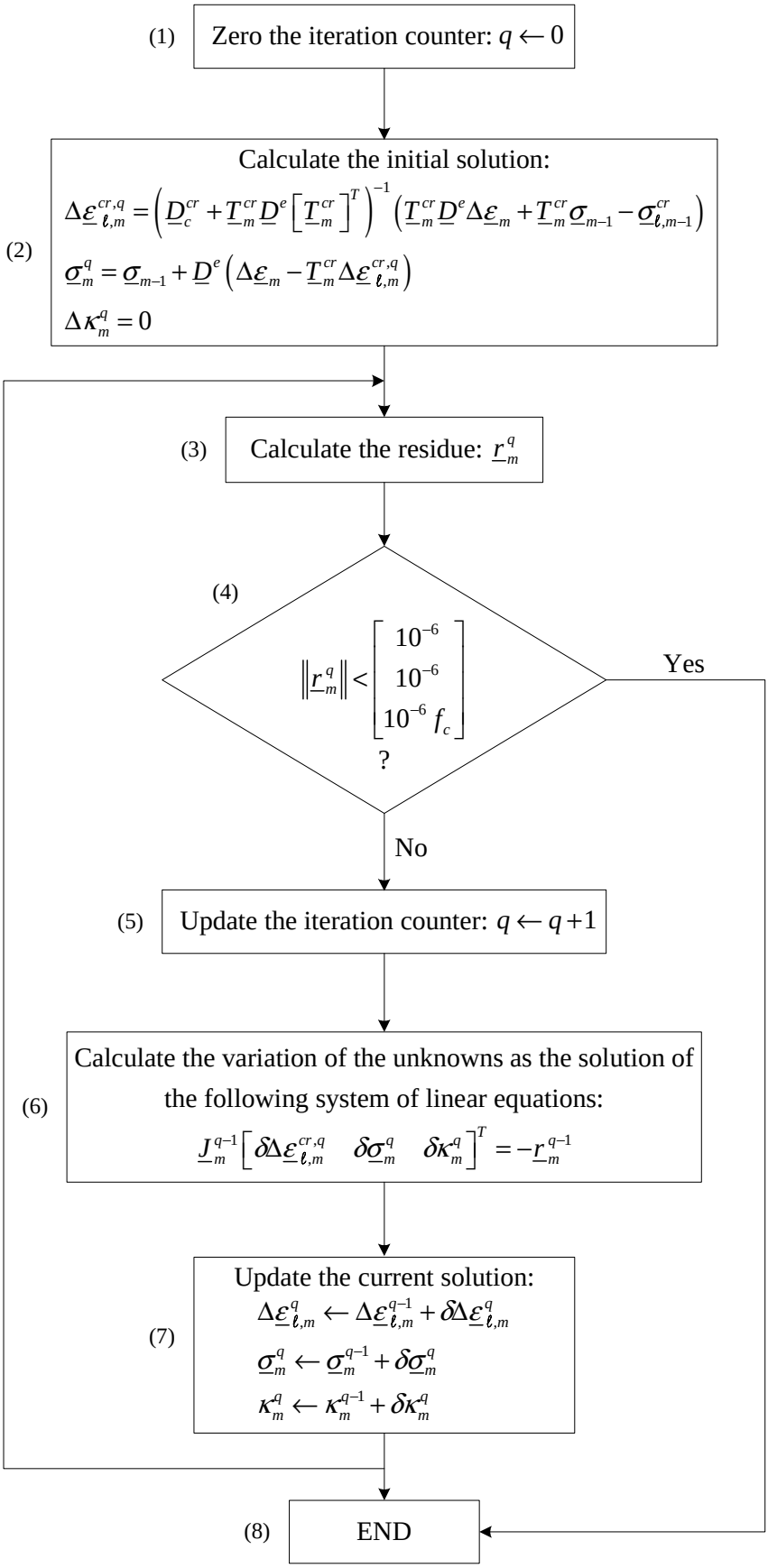

Figure 23 – Returning mapping algorithm of the elasto-plastic multi-fixed smeared crack model.

$$\frac{\partial \underline{f}_1}{\partial \Delta \underline{\varepsilon}_\ell^{cr}} = \frac{\partial \Delta \underline{\sigma}_\ell^{cr}}{\partial \Delta \underline{\varepsilon}_\ell^{cr}} + \underline{T}^{cr}\underline{D}^e\left[\underline{T}^{cr}\right]^T$$

$$\frac{\partial \underline{f}_1}{\partial \underline{\sigma}} = \underline{T}^{cr}\underline{D}^e\Delta\kappa\left(\frac{\partial f}{\partial \underline{\sigma}}\left(\frac{\partial h_c}{\partial \underline{\sigma}}\right)^T + h_c\frac{\partial^2 f}{\partial \underline{\sigma}^2}\right) \tag{91}$$

$$\frac{\partial \underline{f}_1}{\partial \kappa} = \underline{T}^{cr}\underline{D}^e\left(h_c + \Delta\kappa\frac{\partial h_c}{\partial \kappa}\right)\frac{\partial f}{\partial \underline{\sigma}}$$

$$\frac{\partial \underline{f}_2}{\partial \Delta \underline{\varepsilon}_\ell^{cr}} = \left[\underline{T}^{cr}\right]^T$$

$$\frac{\partial \underline{f}_2}{\partial \underline{\sigma}} = \left[\underline{D}^e\right]^{-1} + \Delta\kappa\left(h_c\frac{\partial^2 f}{\partial \underline{\sigma}^2} + \frac{\partial f}{\partial \underline{\sigma}}\left(\frac{\partial h_c}{\partial \underline{\sigma}}\right)^T\right) \tag{92}$$

$$\frac{\partial \underline{f}_2}{\partial \kappa} = \left(h_c + \Delta\kappa\frac{\partial h_c}{\partial \kappa}\right)\frac{\partial f}{\partial \underline{\sigma}}$$

$$\frac{\partial f_3}{\partial \Delta \underline{\varepsilon}_\ell^{cr}} = \underline{0}^T$$

$$\frac{\partial f_3}{\partial \underline{\sigma}} = \left(\frac{\partial f}{\partial \underline{\sigma}}\right)^T \tag{93}$$

$$\frac{\partial f_3}{\partial \kappa} = \frac{\partial f}{\partial \kappa}$$

These derivatives are defined in Sections 2.3.1 and 3.4.3. In the present model $\partial h_c / \partial \kappa = 0$.

4.2.4 Method proposed by de Borst and Nauta

An additional algorithm was implemented and to be used when the algorithm of Figure 23 fails. This algorithm is called was proposed by de Borst and Nauta (1985). In the method proposed by de Borst and Nauta the constitutive equations of the smeared crack model and the constitutive equations of the elasto-plastic model are solved separately. To solve the constitutive equations of the smeared crack model, the procedure described in Section 2.3.1 was used, replacing $\Delta\underline{\varepsilon}$ by $\Delta\underline{\varepsilon} - \Delta\underline{\varepsilon}^p$. The constitutive equations of the elasto-plastic model are solved using the procedure described in Section 3.4.3 for the elasto-plastic model, replacing $\Delta\underline{\varepsilon}$ by $\Delta\underline{\varepsilon} - \Delta\underline{\varepsilon}^{cr}$. Figure 24 shows the implemented

algorithm. The determination of the initial solution is based on the assumption of null plastic flow (see step 2). The solution is reached when the yield surface is not violated (step 4).

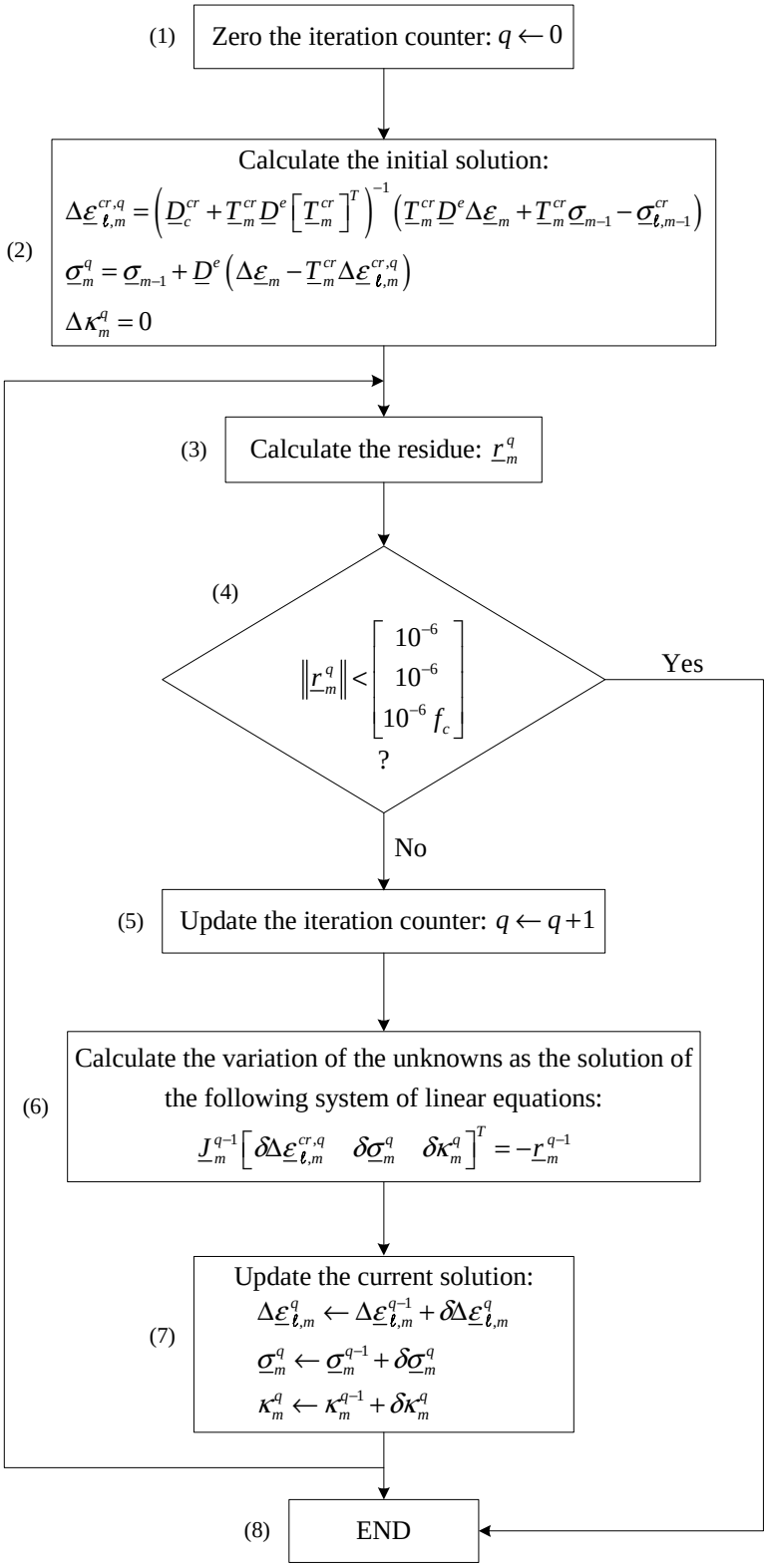

Figure 24 – Method proposed by de Borst and Nauta (1985).

4.3 Consistent tangent constitutive matrix

The elasto-plastic cracked consistent tangent operator, $\underline{D}^{epcr}$, can be calculated from the elasto-plastic consistent tangent constitutive matrix $\underline{D}^{ep}$ (see Section 3.4.4) and from the constitutive matrix of cracked concrete, $\underline{D}^{crco}$ (see Section 2.1.4). The incremental stress vector, $\Delta\underline{\sigma}$, is obtained with

$$\Delta\underline{\sigma} = \underline{D}^{ep}\Delta\underline{\varepsilon}^{ep} \tag{94}$$

where $\underline{D}^{ep}$ is the elasto-plastic consistent tangent constitutive matrix, and $\Delta\underline{\varepsilon}^{ep}$ is the incremental elasto-plastic strain vector, which includes the elastic and the plastic variations of the strain vector ($\Delta\underline{\varepsilon}^{e} + \Delta\underline{\varepsilon}^{p}$). Incorporating equation (78) into (94) and using (5) yields

$$\Delta\underline{\sigma} = \underline{D}^{ep}\left(\Delta\underline{\varepsilon} - \left[\underline{T}^{cr}\right]^{T}\Delta\underline{\varepsilon}_{\ell}^{cr}\right) \tag{95}$$

Pre-multiplying equation (95) by $\underline{T}^{cr}$ and substituting (8) and (11) in the left side of (95), an expression that evaluates the incremental crack strain vector from the incremental cracked concrete strain vector is obtained,

$$\Delta\underline{\varepsilon}_{\ell}^{cr} = \left(\underline{D}^{cr} + \underline{T}^{cr}\underline{D}^{ep}\left[\underline{T}^{cr}\right]^{T}\right)^{-1}\underline{T}^{cr}\underline{D}^{ep}\Delta\underline{\varepsilon} \tag{96}$$

Including (96) in (95) the constitutive law for cracked concrete is obtained

$$\Delta\underline{\sigma} = \left(\underline{D}^{ep} - \underline{D}^{ep}\left[\underline{T}^{cr}\right]^{T}\left(\underline{D}^{cr} + \underline{T}^{cr}\underline{D}^{ep}\left[\underline{T}^{cr}\right]^{T}\right)^{-1}\underline{T}^{cr}\underline{D}^{ep}\right)\Delta\underline{\varepsilon} \tag{97}$$

or

$$\Delta\underline{\sigma} = \underline{D}^{epcr}\Delta\underline{\varepsilon} \tag{98}$$

where $\underline{D}^{epcr}$ is the constitutive matrix for the elasto-plastic cracked concrete

$$\underline{\underline{D}}^{epcr} = \underline{\underline{D}}^{ep} - \underline{\underline{D}}^{ep}\left[\underline{\underline{T}}^{cr}\right]^{T}\left(\underline{\underline{D}}^{cr} + \underline{\underline{T}}^{cr}\underline{\underline{D}}^{ep}\left[\underline{\underline{T}}^{cr}\right]^{T}\right)^{-1}\underline{\underline{T}}^{cr}\underline{\underline{D}}^{ep} \tag{99}$$

4.4 Model appraisal

The first part of this section describes some numerical tests that have the main purpose of evaluating the performance of the model under cyclic loading, inducing different crack statuses and irreversible deformations. In the second part, the performance of the developed elasto-plastic multi-fixed smeared crack model is assessed using results available from the literature.

4.4.1 Numerical tests

The numerical tests were performed using one single 4-node Lagrangian plane stress element with 1×1 Gauss-Legendre integration scheme. Table 7 shows the adopted parameters. Three numerical tests were selected from all that were carried out during the developing phase of the model. In the remaining part of this section a description of these tests is performed.

Table 7 – Concrete properties used in the simulation of the numerical tests.

Poisson's ratio	$\nu_c = 0.20$
Initial Young's modulus	$E_c = 33550.0$ N/mm^2
Compression strength	$f_c = 38.0$ N/mm^2
Strain at peak compression stress	$\varepsilon_1 = 2.2\times10^{-3}$
Parameter defining the initial yield surface	$\alpha_0 = 0.3$
Tensile strength	$f_{ct} = 2.9$ N/mm^2
Type of softening diagram	*Exponential*
Fracture energy	$G_f = 0.005$ N/mm
Shear retention factor	*Exponential* ($p_2 = 2$)
Crack band-width	*Square root of the area of the element*

Traction-Compression-Traction (TCT) numerical test

In the first uniaxial test, the element is, initially, submitted to a tensile force up to the formation of a single crack (steps 1 and 2 in Figure 25). With the purpose of inducing plastic deformation under compression, compressive forces are applied (step 3 and 4). In the beginning of the compression softening phase response, the loading direction is reversed causing a return to the crack-opening process (steps 5 and 6). The loading procedure is terminated at step 7, which corresponds to a complete dissipation of the fracture energy (*fully open* crack status). Figure 25 shows the obtained response in terms of principal stress *versus* principal strain relationship.

Compression-Traction-Compression (CTC) numerical test

This uniaxial test consists on, firstly, submitting the element to a compressive force up to the occurrence of plastic deformation under compression (steps 1, 2 and 3 in Figure 26). After wards, loading is reversed and is increased up to crack formation (step 4) and crack propagation (step 5). At the tensile softening phase loading is again reversed until the compressive softening response is reached. Figure 26 shows the obtained response in terms of principal stress *versus* principal strain relationship.

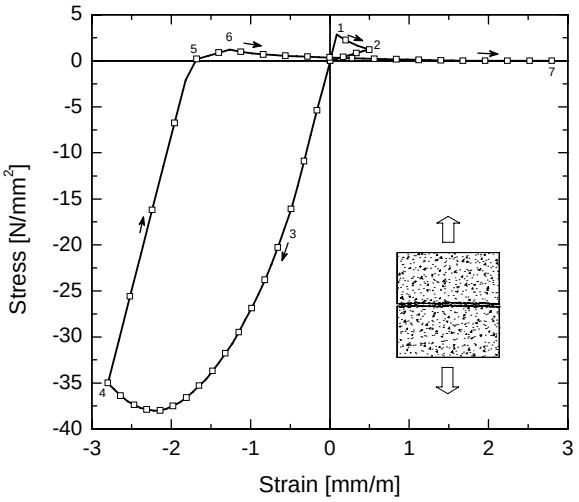

Figure 25 – TCT numerical test.

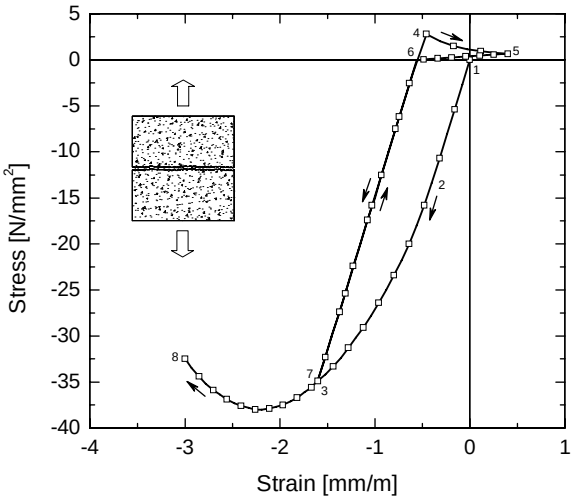

Figure 26 – CTC numerical test.

Biaxial numerical test

The biaxial test consists on the application of biaxial tensile forces up to the formation of two orthogonal cracks (step 1 in Figure 27). After wards, loading in the x_1 direction is

reversed in order to induce compressive forces with the same direction. In the x_2 direction the load continues its progression in the same direction until total dissipation of the fracture energy (step 2 and 3). In step 4, the concrete reached a compressive softening phase (x_1 direction) and the crack orthogonal to x_1 direction remains with *fully open* crack status. Figure 27 shows the obtained response in terms of x_1 and x_2 normal stresses.

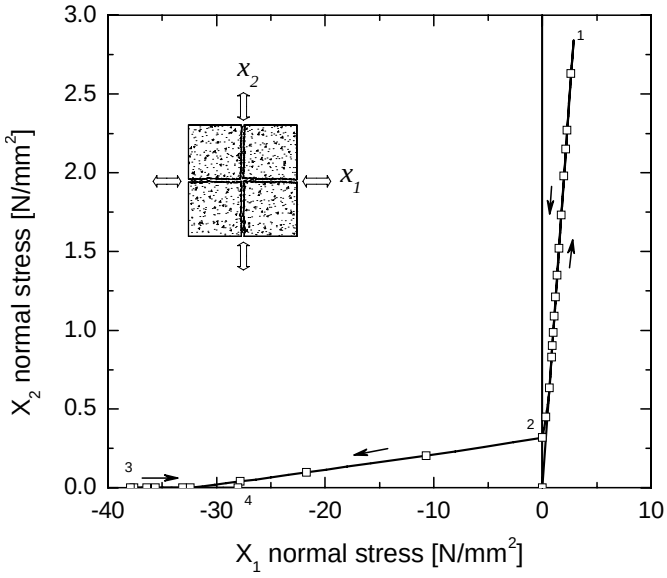

Figure 27 – Biaxial numerical test.

4.4.2 Beam failing by shear

Figure 28 shows the finite element mesh adopted in the simulation of the behavior of the beam tested by Walraven (1978). Due to its load and properties the beam failed by shear. In the simulation, 8-node Serendipity plane stress elements with 3×3 Gauss-Legendre integration scheme were used. Table 8 includes the main properties of the concrete. The properties of the steel reinforcement located in the bottom side of the beam are: Young modulus's $E_s = 210000$ N/mm^2; yield stress $f_{sy} = 440$ N/mm^2.

Some researches have already used this test with the aim of assessing the performance of other models (de Borst and Nauta 1985, Póvoas 1991, Barros 1995). The obtained results indicate that the simulation of beams failing by shear is a difficult task.

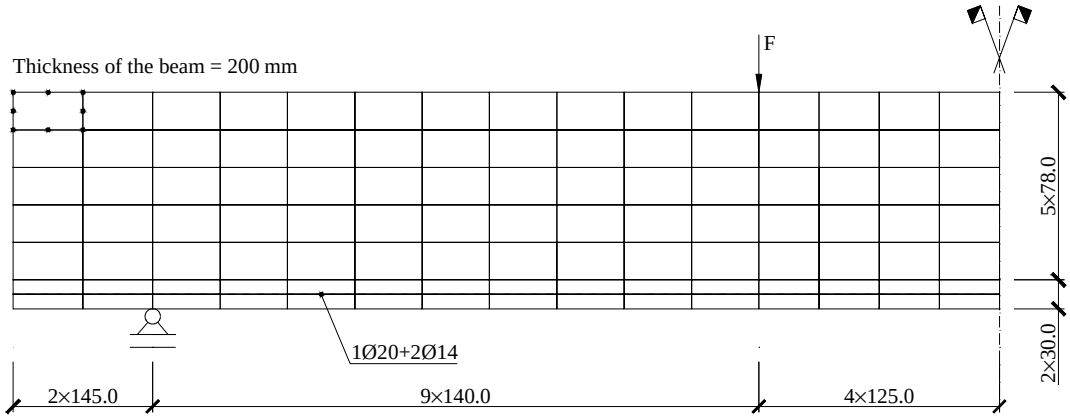

Figure 28 – Finite element mesh of the moderately deep beam.

Table 8 – Concrete properties used in the simulation of the beam failing by shear.

Poisson's ratio	$\nu_c = 0.20$
Initial Young's modulus	$E_c = 28000.0$ N/mm^2
Compression strength	$f_c = 20.0$ N/mm^2
Strain at peak compression stress	$\varepsilon_{c1} = 2.2\times10^{-3}$
Parameter defining the initial yield surface	$\alpha_0 = 0.3$
Tensile strength	$f_{ct} = 2.5$ N/mm^2
Tri-linear softening diagram parameters	$\xi_1 = 0.01$; $\alpha_1 = 0.45$; $\xi_2 = 0.05$; $\alpha_2 = 0.10$
Fracture energy	$G_f = 0.06$ N/mm
Parameter defining the mode I fracture energy available to the new crack	$p_1 = 2$
Shear retention factor	*Exponential* ($p_2 = 2$)
Crack band-width	*Square root of the area of the integration point*
Threshold angle	$\alpha_{th} = 30^o$

Figure 29 and Figure 30 show the experimental and the numerical crack pattern obtained, respectively. A shear crack near the middle of the shear-span of the represented part of the beam can be easily identified. Due to the perfect bond assumed between the reinforcement and the concrete, the numerical model has predicted the formation of cracks at the reinforcement level, which were not observed in the experimental test. Figure 31 includes all cracks and the plastic zones. In some integration points, the concrete is cracked and exhibits plastic deformation, simultaneously.

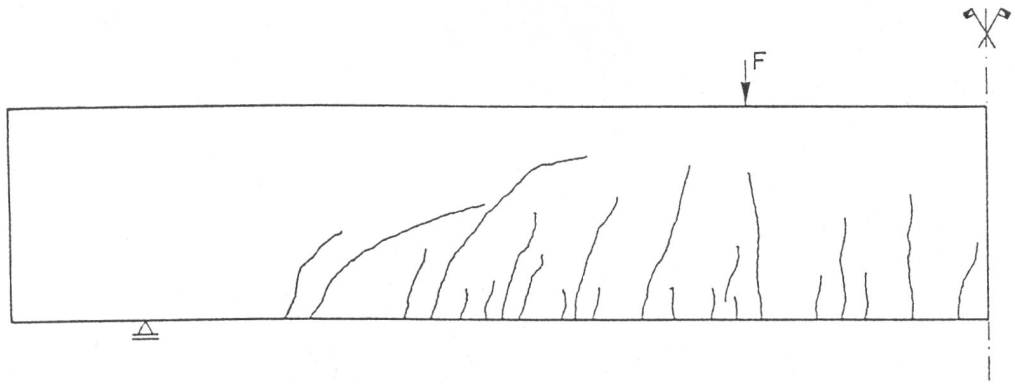

Figure 29 – Experimental crack pattern at impending failure (de Borst and Nauta 1985).

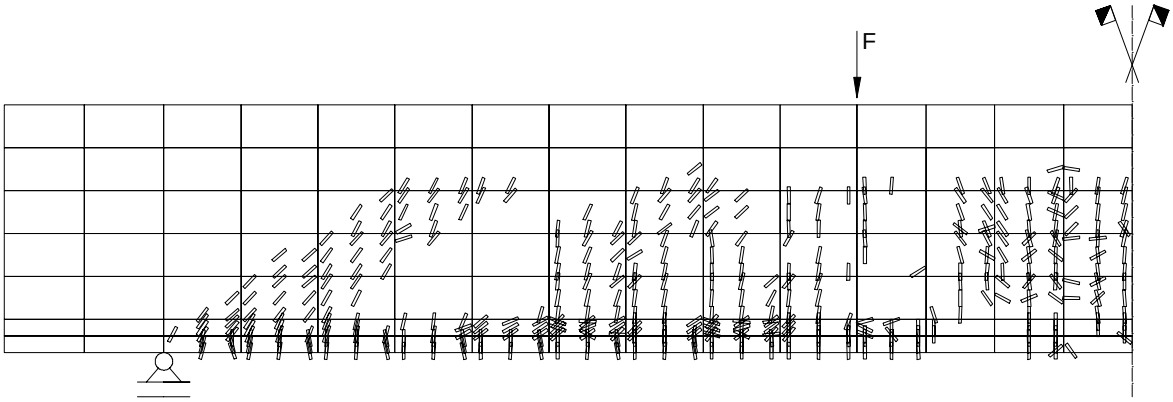

Figure 30 – Numerical crack pattern at the final stage (only cracks with *OPENING* status are included).

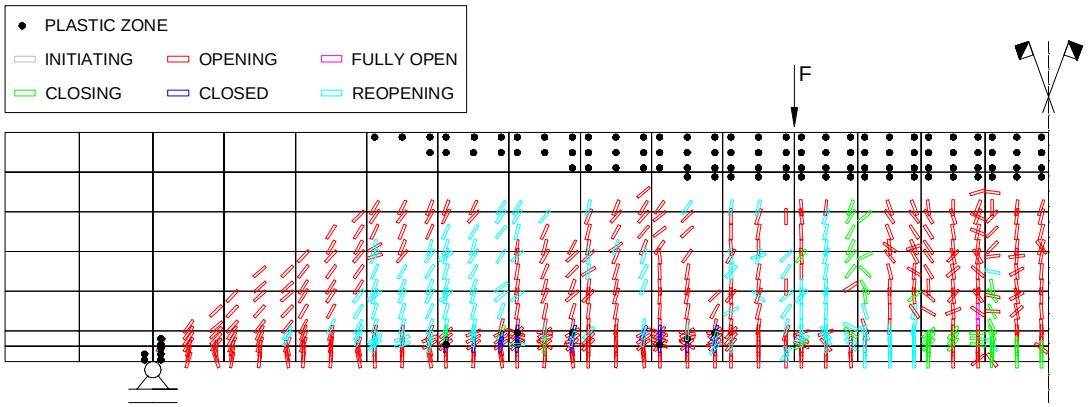

Figure 31 – Numerical crack pattern (all cracks) and plastic zones at the final stage.

Figure 32 shows the relationship between the load and the deflection at mid-span, for both the experimental test and the numerical analysis. A good agreement can be observed with the exception of the ultimate load, which is higher in the numerical simulation. The reason for this behavior is the non-shear failure obtained with the numerical model.

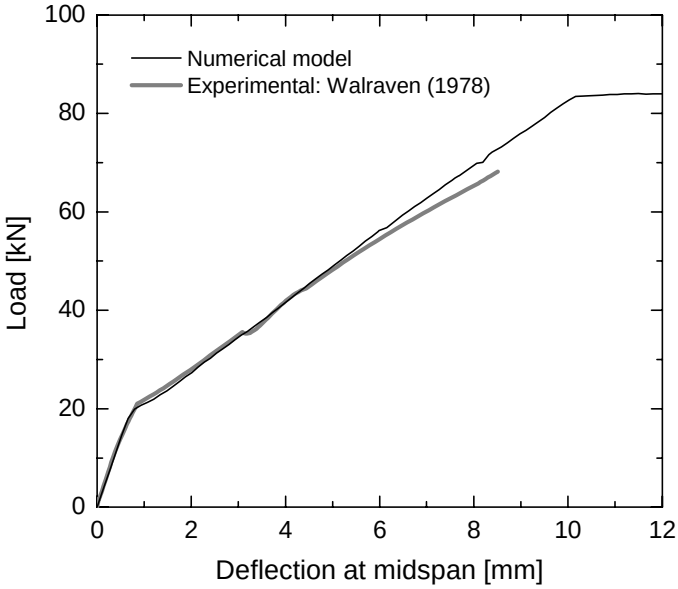

Figure 32 – Load *vs*. deflection at mid-span: experimental and numerical results.

5 CONCLUSIONS

The present report describes the elasto-plastic multi-fixed crack model for concrete developed. This model was implemented in FEMIX computer code.

The formulation of the developed elasto-plastic multi-fixed smeared crack model was described in detail. This model has two independent yield surfaces: one for concrete in tension and the other for concrete in compression. The former controls crack initiation and propagation and the latter controls the plastic behavior of compressed concrete. The incremental strain vector $\Delta\underline{\varepsilon}$ is decomposed in order to accurately simulate the crack status evolution. The post-cracking behavior of concrete depends on the tension-softening diagram. In the developed computer code several alternatives for this diagram are available. Fully implicit Euler backward integration schemes are used to integrate the constitutive equations. Data available in the literature was used to show that the developed model can predict, with enough accuracy, the nonlinear behavior of concrete structures.

REFERENCES

ABAQUS (2002). ABAQUS Theory Manual – version 6.3, US. [available in CD-ROM]

ACI (1991). "Fracture mechanics of concrete: concepts, models and determination of material properties (Reapproved 1999)." *Technical committee document 446.1R-91*, American Concrete Institute (ACI), Committee 446, 146 pp.

ACI (1997). "Finite element analysis of fracture in concrete structures: state-of-the-art." *Technical committee document 446.3R-97*, American Concrete Institute (ACI), Committee 446, 33 pp.

ASCE (1982). "State of the art report on finite element analysis of reinforced concrete." American Society of Civil Engineers (ASCE), ASCE Task Committee on FEA of RC Structures of the Structural Division Committee on Concrete and Masonry Structures, New York, US, 553 pp.

Azevedo, A.F.M. (1985). "Análise não linear de estruturas planas de betão armado pelo método dos elementos finitos. *Nonlinear analysis of plane reinforced concrete structures by the finite element method*." *MSc Thesis*, Faculty of Engineering, University of Porto, Portugal. [in Portuguese]

Azevedo, A.F.M., Barros, J.A.O., Sena-Cruz, J.M. e Gouveia, A.V. (2003). "Software no ensino e no projecto de estruturas. *Educational software for the design of structures.*" *Proceedings of III Congresso de Luso-Moçambicano de Engenharia*, J.S. Gomes, C.F. Afonso, C.C. António and A.S. Matos (eds.), Maputo, Mozambique, 81-92. [in Portuguese]

Barros, J.A.O. (1995). "Comportamento do betão reforçado com fibras. Análise experimental e simulação numérica. *Behavior of fiber reinforced concrete. Experimental analysis and numerical simulation.*" *PhD Thesis*, Faculty of Engineering, University of Porto, Portugal. [in Portuguese]

Bazant, Z.P., and Gambarova, P. (1980). "Rough cracks in reinforced concrete." *Journal of Structural Division*, ASCE, 106(4), 819-842.

Bazant, Z.P., and Oh, B.H. (1983). "Crack band theory for fracture of concrete." *Materials and Structures*, RILEM, 16(93), 155-177.

Bittencourt, T., Ingraffea, A.R., and Llorca, J. (1992). "Simulation of arbitrary, cohesive crack propagation." *Proceedings of the Conference Fracture Mechanics of Concrete Structures*, Z. Bazant (ed.), Elsevier, New York, 339-350.

Cachim, P.B. (1999). "Experimental and numerical analysis of the behavior of structural concrete under fatigue loading with applications to concrete pavements." *PhD Thesis*, Faculty of Engineering, University of Porto, Portugal.

CEB-FIB (1993). "CEB-FIP Model Code 1990 - Design Code." *Thomas Telford*, Lausanne, Switzerland.

Cervenka, V., Pukl, H. and Eligehausen R. (1990). "Computer simulation of anchoring technique and design of concrete structures." *Proceedings of the 2nd International Conference on Computer Aided Analysis and Design of Concrete Structures*, N. Bicanic and H. Mang (eds.), Zell am See, Austria, 1-19.

Chapra, S.C., and Canale, R.P. (1998). "Numerical methods for engineers (Third edition)." *WCB/McGraw-Hill*, Sigapore.

Chen, W.F. (1982). "Plasticity in reinforced concrete." *McGraw-Hill*, New York, US.

Chen, W.F., and Han, D.J. (1988). "Plasticity for structural engineers." *Springer-Verlag*, New York, US.

Chen, W.F., and Mizuno, E. (1990). "Non-linear analysis in soil mechanics. Theory and implementation." *Elsevier*, Amsterdam, The Netherlands.

Cornelissen, H.A.W., Hordijk, D.A., and Reinhardt, H.W. (1986). "Experimental determination of crack softening characteristics of normalweigth and lightweight concrete." *Heron*, Fracture Mechanics and Structural Aspects of Concrete, 31(2), 45-56.

Crisfield, M.A. (1997). "Non-linear finite element analysis of solids and structures. Volume 2: advanced topics." *John Wiley & Sons*, Chichester, England.

Crisfield, M.A., and Wills, J. (1989). "Analysis of R/C panels using different concrete models." *Journal of Engineering Mechanics*, ASCE, 115(3), 578-597.

Dahlblom, O., and Ottosen, N.S. (1990). "Smeared crack analysis using generalized fictitious crack model." *Journal of Engineering Mechanics*, ASCE, 116(1), 55-76.

de Borst, R. (1991). "Computational methods in non-linear solid mechanics. Part 2: physical non-linearity." *Report No. 25-2-91-2-06*, Delft University of Technology, The Netherlands, 174 p.

de Borst, R., and Feenstra, P.H. (1990). "Studies in anisotropic plasticity with reference to Hill criterion." *International Journal of Numerical Methods in Engineering*, 29, 315-336.

de Borst, R., and Nauta, P. (1985). "Non-orthogonal cracks in smeared finite element model." *Engineering Computations Journal*, 2, 35-46.

Feenstra, P.H. (1993). "Computational aspects of biaxial stress in plain and reinforced concrete." *PhD Thesis*, Delft University of Technology, The Netherlands.

Hill, R. (1950). "The mathematical theory of plasticity." *Oxford University Press*, London.

Hillerborg, A., Modéer, M., and Petersson, P.E. (1976). "Analysis of crack formation and crack growth in concrete by means of fracture mechanics and finite elements." *Cement and Concrete Research*, 6, 773-782.

Hodge, P.G. (1957). Discussion [of Prager (1956)]. *Journal of Applying Mechanics*, 23, 482-484.

Hofstetter, G., and Mang, H.A. (1995). "Computational mechanics of reinforced concrete structures." *Friedr. Vieweg & Sohn Verlagsgesellschaft mbH*, Germany.

Hordijk, D.A. (1991). "Local approach to fatigue of concrete." *PhD Thesis*, Delft University of Technology, The Netherlands.

Kormeling, H.A., and Reinhardt, H.W. (1983). "Determination of the fracture energy of normal concrete and epoxy modified concrete." *Report No. 5-83-18*, Stevin Laboratory, Delft University of Technology, The Netherlands.

Kupfer, H., Hilsdorf, H.K., and Rusch, H. (1969). "Behavior of concrete under biaxial stresses." *ACI Journal*, 66(8), 656-666.

Leibengood, L., Darwin, D., and Dodds, R.H. (1986). "Parameters affecting FE analysis of concrete structures." *Journal of Structural Engineering*, ASCE, 112, 326-341.

Lemaitre, J., and Caboche, J.L. (1985). "Mécanique des materieux solides." *Dunod*, Paris, France.

Litton, R.W. (1974). "A contribution to the analysis of concrete structures under cyclic loading." *PhD Thesis*, University of California, Berkeley, US.

Lourenço, P.B. (1996). "Computational strategies for masonry structures." *PhD Thesis*, Delft University of Technology, The Netherlands.

Lubliner, J. (1990). "Plasticity theory." *Macmillan Company*, New York, US.

Ngo, D., and Scordelis, A.C. (1967). "Finite element analysis of reinforced concrete beams." *Journal of the American Concrete Institute*, 64(3), 152-163.

Odqvist, F.K.G. (1933). "Die verfestigung von flusseisenahnlichen korpen. Ein beitrag zur plastizitiitstheorie." *Zeit. Angew. Math. Und Mech.*, 13, 360-3.

Oliver, J., Cervera, M., Oller, S., and Lubliner, J. (1990). "Isotropic damage models and smeared crack analysis of concrete." *Proceedings of the 2nd International Conference on Computer Aided Analysis and Design of Concrete Structures*, N. Bicanic, and H. Mang (eds.), Pineridge Press Ltd, 945-957.

Oñate, E., Oller, S., Oliver, J., and Lubliner, J. (1987). "A constitutive model for cracking of concrete based on the incremental theory of plasticity." *Proceedings of the International Conference in Computational Plasticity-Models*, Software and Apllications, D.R. Owen, E. Hinton, and E. Oñate (eds.), Barcelona, Spain, 1311-1329.

Ortiz, M., and Popov, E.P. (1985). "Accuracy and stability of integration algorithms for elastoplastic constitutive equations." *International Journal of Numerical Methods in Engineering*, 29, 1561-1576.

Owen, D.R.J., and Figueiras, J.A. (1983). "Anisotropic elasto-plastic finite element analysis of thick and thin plates and shells." *International Journal for Numerical Methods in Engineering*, 19, 323-350.

Owen, D.R.J., and Hinton, E. (1980). "Finite elements in plasticity. Theory and practice." *Pineridge Press Limited*, Swansea, UK.

Póvoas, R.H.C.F. (1991) "Modelos não-lineares de análise e dimensionamento de estruturas laminares de betão incluindo efeitos diferidos. *Nonlinear models for the analysis and design of concrete laminate structures including time dependent effects.*" *PhD Thesis*, Faculty of Engineering, University of Porto, Portugal. [in Portuguese]

Prager, W. (1955). "The theory of plasticity: a survey of recent achievements." *Proceedings of the Institute of Mechanical Engineers*, London, England, 169, 41-57.

Rots, J.G. (1988). "Computational modeling of concrete fracture." *PhD Thesis*, Delft University of Technology, The Netherlands.

Rots, J.G. (1992). "Removal of finite elements in smeared crack analysis." *Proceedings of the 3rd International Conference on Computational Plasticity*, Fundamentals and Applications, D.R.J. Owen, E. Oñate, and E. Hinton (eds.), Pineridge Press, 669-680.

Rots, J.G., Nauta, P., Kusters; G.M.A., and Blaawendraad, J. (1985). "Smeared crack approach and fracture localization in concrete." *HERON*, 30(1), 1-48.

Schellekens, J.C.J., and de Borst, R. (1990). "The use of the Hoffmann yield criterion in finite element analysis of anisotropic composites." *Computers & Structures*, Elsevier, 37(6), 1087-1096.

Simo, J.C., and Hughes, T.J.R. (1988). "Elastoplasticity and viscoplasticity – Computational aspects." *Springer*, New York, US.

Simo, J.C., and Taylor, R.L. (1985). "Consistent tangent operators for rate independent elasto-plasticity." *Computer Methods in Applied Mechanics and Engineering*, 48, 101-118.

Van Mier, J.G.M. (1984). "Strain-softening of concrete under multiaxial loading conditions." *PhD Thesis*, Delft University of Technology, The Netherlands.

Walraven, J.C. (1978). "The influence of depth on the shear strength of light-weight concrete beams without shear reinforcement." *Report No. 5-78-4*, Stevin Laboratory, Delft University of Technology, Delft, The Netherlands.

APPENDIX I: HARDENING/SOFTENING LAW FOR CONCRETE

The expression that defines the hardening behavior is the following (see also Figure 18)

$$\bar{\sigma}_1(\kappa) = \bar{\sigma}_0 + (\bar{\sigma}_p - \bar{\sigma}_0)\left(\frac{2\kappa}{\kappa_p} - \frac{\kappa^2}{\kappa_p^2}\right)^{-1/2} \tag{100}$$

The first branch of the softening phase is defined by

$$\bar{\sigma}_2(\kappa) = \frac{-H + \sqrt{H^2 - 4GI}}{2G} \tag{101}$$

where

$$\begin{aligned} G &= \frac{C}{E_c} + \frac{Bf_c}{E_c^2} \\ H &= 1 - A\frac{f_c}{E_c} + \left(C + 2B\frac{f_c}{E_c}\right)\kappa \\ I &= Bf_c\kappa^2 - Af_c\kappa \end{aligned} \tag{102}$$

and

$$\begin{aligned} A &= \frac{E_c}{f_c} \\ B &= \frac{1}{\varepsilon_{c1}^2} \\ C &= \left(\frac{E_c\varepsilon_{c1}}{f_c} - 2\right)\Big/\varepsilon_{c1} \end{aligned} \tag{103}$$

The second branch of the softening phase is defined by

$$\bar{\sigma}_3(\kappa) = \bar{\sigma}_3^3\frac{D}{E_c^2} + \bar{\sigma}_3^2\left(\frac{F}{E_c} + \frac{2D\kappa}{E_c}\right) + \bar{\sigma}_3\left(D\kappa^2 + F\kappa\right) - f_c = 0 \tag{104}$$

where

$$D = \left(\frac{\xi}{\varepsilon_{c,\lim} / \varepsilon_{c1}} - \frac{2}{\left(\varepsilon_{c,\lim} / \varepsilon_{c1} \right)^2} \right) \frac{1}{\varepsilon_{c1}^2}$$
$$F = \left(\frac{4}{\varepsilon_{c,\lim} / \varepsilon_{c1}} - \xi \right) \frac{1}{\varepsilon_{c1}} \tag{105}$$

and

$$\xi = \frac{4 \left[\left(\frac{\varepsilon_{c,\lim}}{\varepsilon_{c1}} \right)^2 \left(\frac{E_c \varepsilon_{c1}}{f_c} - 2 \right) + 2 \frac{\varepsilon_{c,\lim}}{\varepsilon_{c1}} - \frac{E_c \varepsilon_{c1}}{f_c} \right]}{\left[\frac{\varepsilon_{c,\lim}}{\varepsilon_{c1}} \left(\frac{E_c \varepsilon_{c1}}{f_c} - 2 \right) - 1 \right]^2}$$
$$\varepsilon_{c,\lim} = \varepsilon_{c1} \left\{ \frac{1}{2} \left(\frac{1}{2} \frac{E_c \varepsilon_{c1}}{f_c} + 1 \right) + \left[\frac{1}{4} \left(\frac{1}{2} \frac{E_c \varepsilon_{c1}}{f_c} + 1 \right)^2 - \frac{1}{2} \right]^{1/2} \right\} \tag{106}$$

Finally, ε_{c1} is the strain at the uniaxial peak compressive stress, f_c, and E_c is the initial Young's modulus of concrete.

APPENDIX II: CONSISTENT TANGENT OPERATOR

The derivation of the consistent elasto-plastic tangent matrix requires the determination of the total differentials $d\underline{\sigma}_n$, $d\underline{\varepsilon}_n^p$ and df_n (Simo and Hughes 1988), obtained from the constitutive equation (63), the plastic flow (70) and the yield condition (64), respectively, resulting

$$d\underline{\sigma} = \underline{D}^e \left(d\underline{\varepsilon} - d\underline{\varepsilon}^p \right) \tag{107}$$

$$d\underline{\varepsilon}^p = h_c d\lambda \frac{\partial f}{\partial \underline{\sigma}} + h_c \Delta\lambda \frac{\partial^2 f}{\partial \underline{\sigma}^2} d\underline{\sigma} \tag{108}$$

$$df = \left(\frac{\partial f}{\partial \underline{\sigma}} \right)^T d\underline{\sigma} - \frac{\partial \bar{\sigma}}{\partial \kappa} d\kappa = 0 \tag{109}$$

Incorporating equation (108) into (107) yields

$$d\underline{\sigma} = \underline{H} \left(d\underline{\varepsilon} - h_c d\lambda \frac{\partial f}{\partial \underline{\sigma}} \right) \tag{110}$$

where

$$\underline{H} = \left(\left[D^e \right]^{-1} + h_c \Delta\lambda \frac{\partial^2 f}{\partial \underline{\sigma}^2} \right)^{-1} \tag{111}$$

Including equation (110) in equation (109), results

$$\left(\frac{\partial f}{\partial \underline{\sigma}} \right)^T \underline{H} d\underline{\varepsilon} - h_c d\lambda \left(\frac{\partial f}{\partial \underline{\sigma}} \right)^T \underline{H} \frac{\partial f}{\partial \underline{\sigma}} - \frac{\partial \bar{\sigma}}{\partial \kappa} d\kappa = 0 \tag{112}$$

and assuming the strain hardening hypotheses ($d\lambda = d\kappa$), leads to

$$d\lambda = \frac{\left(\frac{\partial f}{\partial \underline{\sigma}}\right)^T \underline{H}}{\frac{\partial \bar{\sigma}}{\partial \kappa} + h_c \left(\frac{\partial f}{\partial \underline{\sigma}}\right)^T \underline{H} \frac{\partial f}{\partial \underline{\sigma}}} d\underline{\varepsilon} \tag{113}$$

Substituing this equation into (110) yields

$$d\underline{\sigma} = \left(\underline{H} - \frac{h_c \underline{H} \frac{\partial f}{\partial \underline{\sigma}} \left(\frac{\partial f}{\partial \underline{\sigma}}\right)^T \underline{H}}{\frac{\partial \bar{\sigma}}{\partial \kappa} + h_c \left(\frac{\partial f}{\partial \underline{\sigma}}\right)^T \underline{H} \frac{\partial f}{\partial \underline{\sigma}}} \right) d\underline{\varepsilon} \tag{114}$$

or

$$d\underline{\sigma} = \left(\underline{H} - \frac{h_c \underline{H} \frac{\partial f}{\partial \underline{\sigma}} \left(\frac{\partial f}{\partial \underline{\sigma}}\right)^T \underline{H}}{h + h_c \left(\frac{\partial f}{\partial \underline{\sigma}}\right)^T \underline{H} \frac{\partial f}{\partial \underline{\sigma}}} \right) d\underline{\varepsilon} \tag{115}$$

where h is the hardening modulus. Finally, the consistent tangent stiffness matrix, $\underline{D}^{ep}$, is given by

$$\underline{D}^{ep} = \underline{H} - \frac{h_c \underline{H} \frac{\partial f}{\partial \underline{\sigma}} \left(\frac{\partial f}{\partial \underline{\sigma}}\right)^T \underline{H}}{h + h_c \left(\frac{\partial f}{\partial \underline{\sigma}}\right)^T \underline{H} \frac{\partial f}{\partial \underline{\sigma}}} \tag{116}$$